

1 **The regime of aerosol asymmetry parameter over**
2 **Europe, Mediterranean and Middle East based on**
3 **MODIS satellite data: evaluation against surface**
4 **AERONET measurements**

5

6 **M. B. Korras-Carraca¹, N. Hatzianastassiou^{2,*}, C. Matsoukas¹, A.**
7 **Gkikas^{3,2}, C. D. Papadimas²**

8 [1]{Department of Environment, University of the Aegean, 81100 Mytilene, Greece }

9 [2]{Laboratory of Meteorology, Department of Physics, University of Ioannina,
10 45110 Ioannina, Greece }

11 [3]{Earth Sciences Department, Barcelona Supercomputing Center, Barcelona,
12 Spain }

13

14 Correspondence to: N. Hatzianastassiou (nhatzian@cc.uoi.gr)

15

16 **Abstract**

17 Atmospheric particulates are a significant forcing agent for the radiative energy
18 budget of the Earth-atmosphere system. The particulates' interaction with radiation,
19 which defines their climate effect, is strongly dependent on their optical properties. In
20 the present work, we study one of the most important optical properties of aerosols,
21 the asymmetry parameter (g_{aer}), over sea surfaces of the region comprising North
22 Africa, the Arabian peninsula, Europe, and the Mediterranean basin. These areas are
23 of great interest, because of the variety of aerosol types they host, both anthropogenic
24 and natural. Using satellite data from the collection 051 of MODIS (MODerate
25 resolution Imaging Spectroradiometer, Terra and Aqua), we investigate the spatio-
26 temporal characteristics of the asymmetry parameter. We generally find significant
27 spatial variability, with larger values over regions dominated by larger size particles,
28 e.g. outside the Atlantic coasts of north-western Africa, where desert-dust outflow
29 takes place. The g_{aer} values tend to decrease with increasing wavelength, especially
30 over areas dominated by small particulates. The intra-annual variability is found to be
31 small in desert-dust areas, with maximum values during summer, while in all other
32 areas larger values are reported during the cold season and smaller during the warm.

33 Significant intra-annual and inter-annual variability is observed around the Black Sea.
34 However, the inter-annual trends of g_{aer} are found to be generally small.
35 Although satellite data have the advantage of broad geographical coverage, they have
36 to be validated against reliable surface measurements. Therefore, we compare
37 satellite-measured values with g_{aer} values measured at 69 stations of the global surface
38 AERONET (Aerosol Robotic Network), located within our region of interest. This
39 way, we provide some insight on the quality and reliability of MODIS data. We report
40 generally better agreement at the wavelength of 870 nm (correlation coefficient R up
41 to 0.47), while of all wavelengths the results of the comparison were better for spring
42 and summer.

43

44 **1 Introduction**

45 Atmospheric aerosol particles interact with radiation, mainly the short wave (SW or
46 solar) part of the spectrum, modifying the energy budget of the Earth-atmosphere
47 system. The aerosol effect is either direct, through the scattering and absorption of
48 solar radiation, and thus reducing the incoming solar radiation flux at the surface,
49 indirect, through the modification of cloud properties, or semi-direct, due to the
50 absorption of solar radiation and consequent modification of the atmospheric
51 temperature profile, convection, and cloud properties (e.g. Graßl, 1979; Hansen, 1997;
52 Lohmann and Feichter, 2005).

53 The interaction of particles with the solar flux, which defines their climate role,
54 strongly depends on their optical properties (Hatzianastassiou et al., 2004; 2007),
55 which cannot be covered globally by surface in situ measurements. Besides the
56 aerosol optical depth (AOD), one of the most important optical properties of
57 atmospheric particles, which is used in radiative transfer, climate, and general
58 circulation models, is the asymmetry parameter (g_{aer}). The asymmetry parameter
59 describes the angular distribution of the scattered radiation and determines whether
60 the particles scatter radiation preferentially to the front or back. The globally available
61 satellite based AOD data are considered to a great extent as reliable and adequate, due
62 to significant developments in surface and satellite measurements during the last two
63 decades, and particularly the arrival of MODIS in 2000, which is regarded as one of
64 the most reliable datasets (Bréon et al., 2011; Nabat et al., 2013). On the other hand,
65 despite the important role of the asymmetry parameter, relevant global coverage data
66 are measured only for the few last years, or are available in long-term aerosol

67 climatologies such as Global Aerosol Data Set (GADS, Koepke et al. 1997) and Max
68 Planck Aerosol Climatology (MAC, Kinne et al., 2013). Even so, asymmetry
69 parameter data are usually examined for regions with limited geographical extent and
70 temporal coverage (Di Iorio et al, 2003), without intercomparison between alternative
71 data platforms.

72 The goal of the present work is the study of the spatiotemporal distribution of the
73 aerosol asymmetry parameter, using the most recent data from MODIS (MODerate
74 resolution Imaging Spectroradiometer, collection 051). Emphasis is given to the
75 comparison between the provided MODIS data and respective reliable surface
76 measurements of the global AERONET, in order to gain insight on the quality of the
77 former.

78 For this study we focus on the region defined by latitudes 5°N to 70°N and longitudes
79 25°W to 60°E, including North Africa, the Arabian peninsula, Europe, and the greater
80 Mediterranean basin (Fig. 1). This area is selected because it is of particular scientific
81 interest due to the simultaneous presence of a variety of particles, both natural and
82 anthropogenic (e.g. desert dust, marine, biomass burning, anthropogenic urban /
83 industrial pollution) as shown in previous studies (Lelieveld et al., 2002; Smirnov et
84 al., 2002; Sciare et al., 2003; Pace et al., 2006; Lyamani et al., 2006; Gerasopoulos et
85 al., 2006; Engelstaedter et al., 2006; Satheesh et al., 2006; Kalivitis et al., 2007; Rahul
86 et al., 2008; Kalapureddy et al., 2009; Alonso-Pérez et al., 2012; Zuluaga et al., 2012;
87 Kischka et al., 2014) which makes this area ideal for aerosol studies. The presence of a
88 variety of aerosols in the area is due to the fact that two of the largest deserts of the
89 planet are partly included in our area of interest, i.e. the Arabian desert and the
90 Sahara, while one finds also significant sources of anthropogenic pollution from urban
91 and industrial centres, mainly in the European continent. Moreover, our area of
92 interest and primarily its desert areas are characterised by a large aerosol load (large
93 optical depth, Remer et al. 2008; Ginoux et al. 2012). In addition, significant regions
94 in this area, more specifically the Mediterranean basin and North Africa, are
95 considered climatically sensitive, since they are threatened by desertification (IPCC,
96 2007; 2013). Finally, one more reason for the selection of study area is that the
97 present study complements previous ones made by our team (e.g. Papadimas et al.,
98 2008, 2012; Hatzianastassiou et al., 2009) analysing other key aerosol optical
99 properties, namely AOD, for the same region. This is the first study (to our

100 knowledge) that focuses on asymmetry parameter over a geographically extended
 101 area, while at the same time compares satellite with ground-station data.

102

103 **2 Data**

104 Before presenting the data used in this study, a short introduction of the parameter
 105 studied is given here for readers more or less unfamiliar with it. The asymmetry
 106 parameter (or factor) is defined by:

107

$$108 \quad g = \frac{\bar{\omega}_1}{3} = \frac{1}{2} \int_{-1}^1 P(\cos \Theta) \cos \Theta d \cos \Theta \quad (1)$$

109 where P is the phase function, which represents the angular distribution of the
 110 scattered energy as a function of the scattering angle Θ and it is defined for molecules,
 111 cloud particles, and aerosols. The phase function can be expressed using the Legendre
 112 polynomials $\bar{\omega}_l$ (see Liou, 2002) and $\bar{\omega}_1$ in Eq. (1) stands for $l=1$. The asymmetry
 113 parameter is the first moment of the phase function and it is an important parameter in
 114 radiative transfer. For isotropic scattering, g equals zero, which is the case for
 115 Rayleigh molecular scattering. The asymmetry parameter increases as the diffraction
 116 peak of the phase function sharpens. For Lorenz-Mie type particles, namely for
 117 aerosols and cloud droplets, the asymmetry parameter takes positive values denoting a
 118 relative strength of forward scattering, with values increasing with particle size. It can
 119 also take negative values if the phase function peaks in backward directions (90-
 120 180°). The phase function and its simple expression, the asymmetry parameter, along
 121 with the extinction coefficient (or equivalently the optical depth) and the single
 122 scattering albedo, constitute the fundamental parameters that drive the transfer of
 123 diffuse intensity (Joseph et al., 1976) and are used in modelling. Hence, the
 124 importance of aerosol asymmetry parameter is easily understood for enabling
 125 computations of aerosol radiative properties and effects (e.g. forcings).

126 In this work, we use MODIS aerosol asymmetry parameter (g_{aer}) data, which we
 127 compare with in-situ measurements at AERONET stations. We provide a detailed
 128 description of the utilised data in the following sections.

129

130 **2.1 Satellite MODIS Terra and Aqua data**

131 MODIS is an instrument (radiometer) placed on the polar-orbiting satellites of NASA
132 (National Aeronautics and Space Administration) Terra and Aqua, 705 km from the
133 Earth, in the framework of the Earth Observing System (EOS) programme. Terra was
134 launched on 18 December 1999, while Aqua was launched on 4 May 2002. The two
135 satellites are moving on opposite directions and their equatorial crossing times are at
136 10:30 (Terra) and 13:30 (Aqua). MODIS is recording data in 36 spectral channels
137 between the visible and the thermal infrared (0.44 – 15 μm), while its swath width is
138 of the order of 2330 km, which results in almost full planetary coverage on a daily
139 basis.

140 Aerosol properties are monitored in 7 spectral channels between 0.47 and 2.13 μm
141 and final results are derived through algorithms developed for aerosol quantities both
142 over land and ocean (Kaufman et al., 1997; Tanré et al., 1997; Ichoku et al., 2002;
143 Remer et al., 2005). MODIS data are organised in “collections” and “levels”.
144 Collections comprise data produced by similar versions of the inversion algorithms,
145 with the recent collection “051” including also outputs from the “Deep Blue”
146 algorithm. Levels are characterised by data of different quality analysis and spatial
147 resolution.

148 In this study we use daily MODIS data for the asymmetry parameter (g_{aer}) provided
149 on an $1^\circ \times 1^\circ$ grid (namely 100x100 km), from Collection 051, Level 3. These data
150 were measured at wavelengths 470, 660, and 860 nm, only over oceanic regions, since
151 they were derived through the algorithm “Dark Target” over ocean. These
152 wavelengths were selected in order to match as much as possible those of the
153 available corresponding AERONET g_{aer} product (see sect. 2.2). The period of analysis
154 stretches from 24-2-2000 to 22-9-2010 for MODIS-Terra and from 4-7-2002 to 18-9-
155 2010 for MODIS-Aqua.

156 The MODIS C051 g_{aer} data are a derived product of the MODIS algorithm over
157 ocean. This MODIS algorithm (http://modis.gsfc.nasa.gov/data/atbd/atbd_mod02.pdf,
158 Remer et al., 2006) retrieves as primary products the AOD at 550 nm, the Fine
159 (Mode) Weighting (FW, also known as fraction of fine-mode aerosol type, FMF) and
160 the Fine (f) and Coarse (c) modes used in the retrieval, along with the fitting error (ϵ)
161 of the simulated spectral reflectance. The algorithm reports additional derived
162 parameters, such as the effective radius (r_e) of the combined size distribution, the
163 spectral total, fine and coarse AODs or the columnar aerosol mass concentration.
164 Among them, g_{aer} is also derived and reported at seven (7) wavelengths, 470, 550,

165 660, 860, 1200, 1600 and 2120 nm. The derived parameters are calculated (Levy et
166 al., 2013) from information contained within the look-up table (LUT) and/or other
167 retrieved products. For example, knowing the resulting total AOD and FMF, and
168 which aerosol types were selected (or assumed), one can go back to the LUT, and
169 recover additional information about the retrieved aerosol, such as the g_{aer} . Hence, it
170 should be noted that the derived g_{aer} product is dependent on the used aerosol models
171 (modes), since the algorithm is based on a LUT approach, assuming that one fine and
172 one coarse lognormal aerosol modes can be combined with appropriate weightings to
173 represent the ambient aerosol properties over the target (spectral reflectance from the
174 LUT is compared with MODIS-measured spectral reflectance to find the “best” –
175 least squares – fit, which is the solution to the inversion). In the C051 algorithm there
176 are four fine modes and five coarse modes, for which the spectral (at the
177 aforementioned 7 wavelengths) aerosol asymmetry parameter values are given in
178 Remer et al (2006).

179 We also used Level 3 daily Ångström exponent data from MODIS-Aqua C051, and
180 also spectral aerosol optical depth data from MODIS-Aqua C006 datasets, from which
181 we computed C006 Ångström exponent. These data were used to assess the validity of
182 g_{aer} data and their temporal tendencies, as discussed in section 3.2.3.

183

184 **2.2 Ground based AERONET data**

185 AERONET (Aerosol Robotic NETwork) is a global network of stations focused on
186 the study of aerosol properties. AERONET currently encompasses about 970 surface
187 stations (number continuously evolving) equipped with sun photometers of type
188 CIMEL Electronique 318 A (Holben et al., 1998), which take spectral radiation flux
189 measurements.

190 The optical properties of aerosols are extracted through the application of inversion
191 algorithms (Dubovik and King, 2000). Data are provided on three levels (1.0, 1.5, and
192 2). In the present work, we use the most reliable cloud-screened and quality assured
193 Level 2 data. AERONET calculates the asymmetry parameter at wavelengths 440,
194 675, 870, and 1020 nm. We employ daily Level 2 asymmetry parameter data from 69
195 stations (Fig. 1), contained in our study area (N. Africa, Arabian peninsula, Europe).
196 We choose only coastal stations, in order to maximize the coexistence of satellite
197 marine g_{aer} data with surface data. Also, in order to compare corresponding data

198 between the satellite and station platforms, we perform comparison only for the 440,
199 675 and 870 nm.

200

201 **3 Satellite based results**

202 **3.1 Geographical distributions**

203 The spatial distribution of annual mean values of g_{aer} is given in Fig. 2 separately at
204 the wavelengths 470, 660 and 860 nm. The values are averages over the common
205 period between Terra and Aqua, namely 4 July 2002 till 18 September 2010. A
206 significant spatial variability is evident, with MODIS-Terra values varying within the
207 ranges 0.63 - 0.76, 0.57 – 0.75, and 0.55 – 0.74, at 470, 660 and 860 nm, respectively.
208 The results exhibit a decreasing tendency of g_{aer} with increasing wavelength,
209 consistent with the theory. Similar results are also obtained from MODIS-Aqua, but
210 with slightly smaller values than Terra by up to 0.02 on average. More specifically,
211 the corresponding ranges of wavelengths are 0.63 - 0.75, 0.57 – 0.73, and 0.55 – 0.73.
212 The smaller Aqua than Terra g_{aer} values could be attributed to smaller sizes of
213 aerosols in midday than morning, corresponding to passages of Aqua and Terra,
214 respectively, associated with lower relative humidity values and shrinking of aerosol
215 particles. It should be reminded that the ability of atmospheric aerosol to absorb water
216 affects the particle size (hygroscopic growth), as described by Köhler theory in the
217 early 20th century. It is also well known that relative humidity significantly affects
218 aerosol optical properties (e.g. Pilinis et al., 1996; Kondratyev, 1999), namely AOD,
219 single scattering albedo and g_{aer} , by modifying the aerosol liquid water content, size
220 and hence extinction coefficient and refractive indices.

221 In general, the largest g_{aer} values (deep red colors) are observed off the coasts of West
222 Africa (eastern tropical Atlantic Ocean) at all three wavelengths. High values are also
223 found over the Red and Arabian Seas. These high values are due to strong dust
224 outflows from the Saharan and Arabian deserts carrying out coarse aerosol particles
225 (Prospero et al., 2002; Alonso-Pérez et al., 2012; Miller et al., 2008) and causing
226 strong forward scattering. Nevertheless, the Persian Gulf region, which is surrounded
227 by deserts, is characterized by relatively smaller g_{aer} values. More specifically, values
228 as small as 0.69 (MODIS-Terra) and 0.67 (MODIS-Aqua) are observed in this region
229 at 470 nm, while at the longer wavelengths (660, 860 nm) the smallest values are
230 equal to 0.66 (Terra) and 0.64 (Aqua). The smaller g_{aer} values over the Persian Gulf

231 can be attributed to the presence of fine aerosols, which is corroborated by the low
232 effective radius and large fine-fraction measurements by MODIS over the Persian
233 Gulf, compared to neighbouring areas (not shown here). These fine particles originate
234 from the industrial activities in the Gulf countries related to oilfields or refineries
235 (Goloub and Arino, 2000; Smirnov et al., 2002a,b; Dubovik et al., 2002).

236 The high g_{aer} values over the northeastern tropical Atlantic Ocean as well as west of
237 the Iberian coasts are possibly related with the presence of coarse sea salt particles.
238 On the other hand, the asymmetry parameter takes clearly smaller values over the
239 Black Sea, where according to MODIS-Terra varies between 0.63 and 0.7 at 470 nm,
240 0.57 and 0.67 at 660 nm, and 0.55 and 0.66 at 860 nm, with the smallest values
241 appearing over the Crimean peninsula (corresponding maximum Aqua values are
242 smaller by 0.02). The small Black Sea g_{aer} values can be associated with industrial but
243 also biomass burning activities in nearby countries. A region of special interest is the
244 Mediterranean basin since it hosts a large variety of aerosols like anthropogenic,
245 desert dust or sea salt (e.g. Barnaba and Gobbi, 2004). The MODIS results over this
246 region show relatively small g_{aer} values, secondary to those of Black Sea,
247 characterized by an increase from north to south, which is more evident at 660 and
248 860 nm. More specifically, based on MODIS-Terra, g_{aer} over the Mediterranean takes
249 values from 0.68 to 0.74 at 470 nm, while at 670 and 860 nm it ranges from 0.64 to
250 0.73 and 0.62 to 0.72, respectively. According to MODIS-Aqua the g_{aer} values are
251 slightly smaller again. The observed low values in the northern parts of the
252 Mediterranean are probably associated with the presence of fine anthropogenic
253 aerosols transported from adjacent urban and industrial areas in the north, especially
254 in central Europe. In contrast, the higher g_{aer} values in the southern Mediterranean,
255 particularly near the North African coasts, can be explained by the proximity to the
256 Sahara desert and the frequent transport of significant amounts of coarse dust (e.g.
257 Kalivitis et al., 2006; Hatzianastassiou et al., 2009; Gkikas et al., 2009; 2014).

258 The spatial distributions of climatological monthly mean g_{aer} values from MODIS-
259 Aqua at 470 nm reveal significant differences in the range and the patterns of the
260 seasonal variability, depending on the area (Fig. 3). Thus, in tropical and sub-tropical
261 areas of Atlantic Ocean (up to about 30°N), where dust is exported from Sahara, g_{aer}
262 keeps high values throughout the year, which reach or even exceed 0.74 locally. Over
263 the regions of Arabian and Red Seas and the Gulf of Aden, which also experience
264 desert dust transport, larger g_{aer} values appear in the period from March to September,

265 with a maximum in August (locally as high as 0.75-0.76). This seasonal behavior is in
266 line with intra-annual changes of dust production over the Arabian peninsula indicated
267 by MODIS Ångström Exponent (AE) and Deep Blue aerosol optical depth data
268 (Ginoux et al., 2002), as well as over southwest Asia through in-situ data (Rashki et
269 al., 2012), aerosol index from various platforms and MODIS Deep Blue AOD data
270 (Rashki et al., 2014). Indeed, the production of dust there is relatively poor in winter,
271 increases in March and April and becomes maximum in June and July (Prospero et
272 al., 2002). Over the Arabian Sea, it is known that large amounts of desert dust are
273 carried out during spring and early summer (Prospero et al, 2002; Savoie et al., 1987;
274 Tindale and Pease, 1999; Satheesh et al., 1999). Nevertheless, according to MODIS,
275 the seasonal variability of g_{aer} remains relatively small there in line with a small
276 seasonal variability in MODIS Deep Blue AE data (results of our analysis, not shown
277 here). This can be explained by the presence of sea salt coarse particles throughout the
278 year, with which dust particles co-exist.

279 A greater seasonal variability exists over the Persian Gulf, where g_{aer} values are
280 higher during spring and in particular in summer (up to 0.74 at 470 nm according to
281 Aqua), and smaller in autumn and winter (area-minimum values smaller than 0.65).
282 This seasonal behavior can be explained taking into account the meteorological
283 conditions over the greater area of the Gulf; mainly in spring and summer dry
284 northwestern winds (Shamal) blow from northwest carrying desert dust from the arid
285 areas of Iraq (Heishman 1999; Smirnov et al. 2002a,b; Kutiel and Furman, 2003). The
286 transport of dust is gradually decreased in autumn and reaches its minimum in winter.
287 When the presence of desert dust is limited, a significant fraction of total aerosol load
288 in the region consists of fine anthropogenic particles (Smirnov et al. 2002a,b), which
289 can explain the observed relatively small g_{aer} values in autumn and winter.

290 In the Mediterranean basin g_{aer} exhibits a relatively small seasonal variation, with
291 lower values tending to appear in summer, in line with the presence of fine
292 anthropogenic or biomass burning aerosols in the area, transported from the Balkans
293 or central Europe (Hatzianastassiou et al. et al., 2009). On the contrary, over the Black
294 Sea, a clear seasonal cycle is apparent, with higher values in the cold period of the
295 year and smaller in the warm one. More specifically, according to MODIS-Aqua, the
296 values at 470 nm drop down to 0.61 in summer months whereas they reach 0.7 in
297 January and December. This seasonality is in agreement with the summer biomass

298 burning from agricultural activities and wildfires (Barnaba et al., 2011; Bovchaliuk et
299 al., 2013), and the resulting abundance of fine particles.

300 It is also interesting to look at the geographical distribution of monthly g_{aer} values in
301 latitudes higher than $50^{\circ}N$, for which annual mean values were not given in Fig. 2
302 because of unavailability of data for all months. Off shore northern France (English
303 Channel) and Germany the asymmetry parameter has small seasonally constant values
304 (note that data do not exist for January and February). In these areas, the aerosol load
305 consists mainly of anthropogenic polluted particles, which explains the small g_{aer}
306 values there.

307 In the Baltic Sea (values available from March to October) g_{aer} shows a significant
308 spatial and temporal variability. More specifically, it is small during summer whereas
309 it increases, locally up to more than 0.7, in March and October. The smaller summer
310 values can be explained by the presence of fine aerosols in the Baltic Sea originating
311 from forest fires in Europe and Russia (Zdun et al., 2011). On the contrary, in autumn
312 the local aerosol loading consists largely of coarse marine aerosols. It is also
313 important to note that the Baltic Sea hosts significant amounts of anthropogenic
314 industrial and urban aerosols throughout the year, but especially in summer (Zdun et
315 al., 2011).

316 In the higher latitudes of Atlantic Ocean, where the presence of maritime aerosols is
317 dominant, we note a remarkable month by month variation of asymmetry parameter,
318 with low values in summer (values up to 0.59) against high values (up to 0.75-0.77) in
319 spring (March, April) and autumn (October). This difference is possibly explained by
320 the seasonal variability of aerosol size in the northern Atlantic. Apart from the
321 presence of coarse sea salt throughout the year, in spring and summer small particles
322 are formed through photochemical reactions of dimethylsulphide (DMS) emitted by
323 phytoplankton decreasing the aerosol size. Moreover during summer fine
324 anthropogenic aerosols are transported in the region from North America (Yu, 2003;
325 Chubarova, 2009). These result in lower g_{aer} values between May and August.

326 Based on MODIS-Terra, the patterns of spatial distribution are generally the same
327 with Aqua, with slightly larger g_{aer} values. At larger wavelengths (660, 860 nm) a
328 decrease of g_{aer} is observed, especially for its smallest values. Further details and an
329 overall picture are given in section (3.2.1) which deals with climatological monthly
330 mean values not at the pixel but at the regional level.

331

332 3.2 Temporal variability

333 3.2.1 Seasonal variability

334 In order to provide an easier assessment of the seasonal cycle of aerosol asymmetry
335 parameter and its changes from one region to another, but also among the different
336 wavelengths (470, 660 and 860 nm), the study region was divided in 6 smaller sub-
337 regions (see Fig. 1). The average values of monthly mean climatological data of the
338 pixels found within each sub-region's geographical limits have been computed and
339 are given in Fig. 4, for every wavelength, both for Terra and Aqua. It appears that the
340 seasonal cycle differs between the sub-regions, as it has been already shown in the
341 geographical map distributions discussed in the previous section.

342 At 470 nm (Fig. 4i), the intra-annual variability of g_{aer} is greater over the Black Sea,
343 where it is as large as 0.06 according to MODIS-Terra and 0.05 according to MODIS-
344 Aqua, the north-eastern Atlantic Ocean (0.04 and 0.05 for Terra and Aqua,
345 respectively) and the seas of North Europe (0.05 for both Terra and Aqua). In these
346 regions, there is a tendency for smaller values during summer. More specifically, in
347 the Black Sea the smallest g_{aer} value (0.64) is observed in June, over the seas of North
348 Europe in July and over the north-eastern Atlantic Ocean in August. In these regions,
349 the largest values appear in the cold period of the year. Reverse seasonality with a
350 large seasonal amplitude is observed over the Persian Gulf, where the variability is as
351 large as 0.08, according to both MODIS-Terra and Aqua. The seasonal cycle of g_{aer}
352 over the Middle East exhibits a smaller range of variability (0.02 for MODIS-Terra
353 and 0.03 for Aqua) along with a reverse seasonal variation, with maximum values in
354 summer and minimum in winter. In the other two sub-regions (Mediterranean and
355 eastern Atlantic Ocean) the annual range of values is small (< 0.02). It is noteworthy
356 that in the Mediterranean Sea, there is a weak tendency of appearance of double
357 maxima in winter and spring. The spring maximum should be associated with the
358 presence of desert dust particles, which are transported from Sahara, mainly in the
359 eastern Mediterranean in this season (e.g. Fotiadi et al., 2006; Kalivitis et al., 2007;
360 Papadimas et al. 2008, Gkikas et al. 2009; Hatzianastassiou et al., 2009; Gkikas et al.,
361 2013). There is also a similar transport of Saharan dust in the central and western
362 Mediterranean during summer and autumn (e.g. Gkikas et al., 2009; 2013), but then
363 the predominance is not so clear because of the co-existence of fine anthropogenic
364 aerosols. Regardless of the annual cycle, smaller g_{aer} values are clearly distinguished
365 over the Black Sea and North Europe seas throughout the whole year.

366 At 660 nm, the g_{aer} values are lower than at 470 nm, in particular over Black Sea,
367 North Europe and North-East Atlantic, whereas the intra-annual variability (range of
368 g_{aer} values) increases up to 0.10 (Terra) and 0.08 (Aqua) over the Black Sea. This
369 increase is mainly attributed to the reduction of summer values due to the strong
370 appearance of fine aerosols in this season. Also, at 660 nm, there is a clearer double
371 annual variation of g_{aer} over the Mediterranean Sea than at 470 nm. At 860 nm the
372 general picture is similar to that of 660 nm though a further increase of month by
373 month variability is noticeable.

374 In general, our results indicate that over the regions characterized by a strong presence
375 of desert dust particles (eastern Atlantic and the Middle East and Mediterranean Seas)
376 the annual range of variability of g_{aer} is smaller than in the other regions. An
377 additional feature above regions with desert dust is the smaller decrease of g_{aer} values
378 with increasing wavelengths. This is attributed to the lower g_{aer} spectral dependence
379 of coarse compared to fine particles (e.g. Dubovik et al, 2002; J. Bi et al., 2011).

380 We should note that the MODIS-Terra and Aqua g_{aer} seasonal cycles are about similar
381 but with generally greater Terra than Aqua values.

382 **3.2.2 Inter-annual variability and changes**

383 Figure 5 displays the geographical distribution of the slope of inter-annual trend of
384 g_{aer} over the study region, as computed from the application of the Mann-Kendall test
385 to time series of deseasonalized monthly anomalies of g_{aer} at 470 nm. Results are
386 shown in units decade⁻¹ for both Terra and Aqua over their common time period,
387 namely 2002 – 2010, only if the trend is statistically significant at the 95% confidence
388 level. We also performed the same analysis for the 660 and 860 nm (not shown), with
389 similar results to the 470 nm wavelength.

390 In general, the estimated changes are relatively small. Terra produces widely
391 statistically significant positive trends, showing that during the period of interest, the
392 asymmetry parameter increased over the examined area, with very few exceptions.
393 The results from Aqua are statistically significant at considerably fewer cells, but also
394 give a few points with decreasing g_{aer} . Based on Terra data, the stronger increases are
395 observed in the eastern and southern Black Sea, as well as over the Baltic and Barents
396 Seas. According to MODIS-Aqua, negative trends are found over few Atlantic Ocean
397 cells. Both Aqua and Terra report increases of g_{aer} over the Persian Gulf, the Red Sea,
398 South Black Sea, East Mediterranean, the coast of the Iberian Peninsula, and some

399 coastal areas of West Africa. The differences encountered between the Terra and
400 Aqua g_{aer} trends may be attributed to the different time of passage of each satellite
401 platform carrying the same MODIS instrument, given that everything else is the same.
402 Nevertheless, they may more probably be the result of calibration differences between
403 the two MODIS sensors. It is known that there is a degradation of MODIS sensor
404 (Levy et al., 2010; Lyapustin et al., 2014) impacting time series of MODIS products.
405 More specifically, it is also known that Terra suffers more than Aqua from optical
406 sensor degradation. These calibration issues are known to affect MODIS AOD
407 retrievals, producing an offset between Terra and Aqua, and they are also expected to
408 affect aerosol asymmetry parameter, which is probably more sensitive to such
409 calibration uncertainties than AOD. In this sense, the results of Fig. 5 shown here are
410 not to be taken as truth but rather they are given as a diagnostic of a problematic
411 situation with MODIS aerosol asymmetry parameter inter-annual changes. Such
412 calibration issues are expected to be addressed, at least partly, in the new Collection
413 006 products. Nevertheless, a preliminary comparison between MODIS Aqua C051
414 and C006 Ångström exponent (AE), which is another common aerosol parameter
415 strongly dependent on size, using data for the 550-865 pair of wavelengths spanning
416 the period 2002-2010, does not reveal significant modifications in geographical
417 patterns of AE inter-annual changes. This puts some confidence on the C051 g_{aer}
418 results given in the present study. The results of this analysis are presented in detail in
419 the next sub-section (3.2.3).

420 The overall g_{aer} changes of Fig. 5 may hide smaller timescale variations of g_{aer} , which
421 are obtained by the time-series shown in Fig. 6. Results are given for the 7 sub-
422 regions defined previously, at the three different wavelengths and for Terra and Aqua
423 separately. A general pattern is the decrease of g_{aer} values with increasing wavelength,
424 in particular from 470 to 660 nm. The largest month to month and year to year
425 variation is for Black Sea (Fig. 6i). Relatively large variability is also found in the
426 sub-regions of NE Atlantic (6v), North Europe (6vi) and the Persian Gulf (6vii). On
427 the contrary, small variability is noticed in the eastern Atlantic, where systematic dust
428 outflows from Sahara take place leading to consistently high values of g_{aer} . There are
429 also some other interesting patterns, like the significant drop of g_{aer} with wavelength
430 in areas characterized by the presence of fine aerosols, namely the Black Sea, North
431 Europe and the Persian Gulf (Figs, 6i,vi,vii, respectively). The specific patterns of
432 inter-annual changes of g_{aer} are suggested by both Terra and Aqua, though a slight
433 overestimation by Terra is again apparent in this figure. The obtained results of our

434 analysis are meaningful and in accordance with the theory, underlining the ability of
435 satellite observations to reasonably capture the g_{aer} regime over the studied regions.

436 **3.2.3 Possible uncertainties of MODIS aerosol asymmetry parameter**

437 The MODIS aerosol asymmetry parameter is not a direct product of the MODIS
438 retrieval algorithm, but it is rather a derived by-product. Since this parameter is
439 dependent on aerosol modes used and relative weights, it is understood that there can
440 be uncertainties associated with it. Therefore questions may arise about the validity of
441 g_{aer} and their spatial and temporal patterns presented in the previous sub-sections.
442 Given that, as already mentioned, it is an aerosol optical parameter that is valuable
443 and highly required by radiative transfer and climate models, it is worth assessing it
444 through comparison against another more common aerosol size parameter, namely the
445 C051 MODIS Ångström exponent at the 550-865 nm wavelength pair ($AE_{550-865}$) over
446 ocean, which is an evaluated MODIS aerosol size product (Levy et al., 2010) that is
447 extensively used in literature. Figure 7a, displays the geographical distribution of
448 long-term average AE for the whole study period, i.e. 2002-2010. In this figure, the
449 northernmost areas are blank with respect to g_{aer} (Fig. 7a) because there are no data
450 during winter and a long-term average would be biased. The main geographical
451 patterns in Fig.7a are in line with those of asymmetry parameter (Fig. 2). For
452 example, note the high AE values in the Black Sea (between about 1.3 and 1.8,
453 yellowish-reddish colors), indicative of fine aerosols, the relatively high values in the
454 Mediterranean Sea (between about 0.7 and 1.2, greenish-yellowish colors) and the
455 low values (0.1-0.4, deep bluish colors) off the western African coasts corresponding
456 to exported Saharan dust. Over the same areas, g_{aer} takes inverse low and high values,
457 for example smaller than 0.65 over the Black Sea and larger than 0.7-0.75 off the
458 western African coasts (Figs 2ii-b and 2iii-b), indicating the predominance of fine and
459 coarse aerosols respectively, in accordance with AE. The consistency between g_{aer} and
460 AE data is shown by the strong anti-correlation between the MODIS $AE_{550-865}$ and g_{aer}
461 data at 660 and 860 nm, shown in Figures 7b and 7c, respectively. It should be noted
462 that correlation coefficients are computed from any available data pairs, i.e. available
463 data for both g_{aer} and $AE_{550-865}$ at a given pixel and day. Note that there are no blank
464 areas in Figs 7b and 7c, in contrast to Fig. 7a. There are both AE and g_{aer} data for all
465 seasons except winter and therefore, correlation coefficients can be calculated for
466 these regions. Strong negative correlation coefficients, larger than 0.7 and 0.8 in Figs
467 7b and 7c, respectively, relate inversely high g_{aer} values with low AE ones and vice-

468 versa, over the same areas. In both cases (Figs 7b and 7c), the correlation is slightly
469 higher over sea areas characterized by the presence of fine aerosols (e.g. Black Sea or
470 Persian Gulf) and lower over seas undergoing frequent transport of coarse dust
471 particles (e.g. southern Mediterranean Sea, Arabian Sea or Atlantic Ocean off the
472 western African coasts). The overall computed correlation coefficient between g_{aer} and
473 AE is equal to -0.95 over the Black Sea, -0.89 over the Mediterranean Sea, -0.87 and -
474 0.94 over the Arabian Sea and Persian Gulf, respectively and -0.89 off the western
475 African coasts (values given for $AE_{550-865}$ and g_{aer} data at 860 nm). These results
476 indicate that the spatial patterns of MODIS C051 g_{aer} product are reasonable as
477 compared to the C051 Ångström exponent data. This shows that the use of g_{aer} in
478 modeling studies can be considered as reasonably reliable with regards to the
479 consideration of fine and coarse aerosols over the examined study area, with slightly
480 more confidence over areas characterized by the presence of fine particles, such as the
481 Black Sea or Persian Gulf.

482 Since questions may also arise about possible uncertainties regarding the long-term
483 variability of MODIS C051 aerosol size products, due to the calibration issues
484 discussed in the previous section, the corresponding MODIS C006 AE product is
485 displayed in Fig. 8a. Figs. 8a and 7a are similar in the main geographical patterns of
486 the two collections' AE product. The similarity between C051 and C006 AE data is
487 also depicted in the computed correlation coefficients (Fig. 8b), exceeding 0.8, and
488 biases (in absolute and relative percentage terms, Figs 8c and 8d, respectively). For
489 the Mediterranean Sea, the Arabian Sea and Persian Gulf, biases are smaller than 0.1
490 or 10% in most areas and 0.2 or 20% almost everywhere. Relative biases larger than
491 30% are only observed over the open Atlantic Ocean). The overall computed
492 correlation coefficient for the entire study region is 0.88 (0.86, 0.89, 0.95 and 0.84 for
493 Mediterranean, Arabian, Persian and Atlantic sea surfaces off the western African
494 coasts). The corresponding overall relative percent bias is equal to 15.6% (9.1, 6.7,
495 6.1 and 15.7 for the same sub-areas as above). Our results indicate that the uncertainty
496 related to the use of C051 AE data is small, especially over the Mediterranean Sea, the
497 Arabian Sea, the Persian Gulf and the Atlantic Ocean areas not far from the European,
498 African and Asian coastlines. Our AE results are in line with those of Levy et al.
499 (2013, Fig. 15) which refer, however, only to year 2008 (ours are for 2002-2010). In
500 addition, a comparison is attempted in Figs 8e and 8f between the computed trends of
501 C051 and C006 AE data over the common period 2002-2010, in order to assess
502 whether changes are detected, which could be an indication of possible changes in

503 corresponding asymmetry parameter trends. Figures 8e and 8f show the computed
 504 deseasonalized trends of slope values for both C051 and C006 AE. The results reveal
 505 similar patterns between C051 and C006. Small trends are found in both of them, in
 506 agreement with the small trends of asymmetry parameter reported in Fig. 5. We find
 507 that the sign of AE trends basically does not change from C051 to C006. This might
 508 be a signal that no changes of aerosol asymmetry parameter are expected in C006 and
 509 puts confidence on the C051 results given in the present study.

510

511 **4 Evaluation against AERONET data**

512 In order to evaluate the satellite-measured aerosol asymmetry parameter, we identified
 513 the AERONET stations inside our area of interest and finally utilised only the coastal
 514 ones, so that both satellite and surface data be available. The total number of these
 515 stations is 69, and their locations are shown in Fig. 1 (open and full circles).

516 Table 1 contains the comparison statistical metrics for all wavelengths (Pearson
 517 correlation coefficient, bias, root mean square error (RMSE), slope, intercept) of the
 518 comparison between surface daily mean data from AERONET and satellite data from
 519 MODIS-Terra and MODIS-Aqua, which correspond to the $1^\circ \times 1^\circ$ cell wherein each
 520 station is located. For this analysis, we use all cells and days with common data
 521 between Terra-AERONET and Aqua-AERONET. The mean differences are
 522 calculated as $g_{\text{aer}}(\text{AERONET}) - g_{\text{aer}}(\text{Aqua})$ and $g_{\text{aer}}(\text{AERONET}) - g_{\text{aer}}(\text{Terra})$.

523 In general, we may note that on an annual level, the MODIS-Terra and Aqua
 524 asymmetry parameter values at 470 nm are not in very good agreement with the
 525 respective data from AERONET at 440 nm, while the results at the largest
 526 wavelengths are more reassuring, though not being very satisfactory (increasing R and
 527 decreasing relative bias and RMSE values at 675/660 nm and 870 nm). At 870 nm
 528 (Table 1 and Fig. 9), correlation coefficients are found to be the largest and equal to
 529 0.47 (AERONET-Terra) and 0.46 (AERONET-Aqua), while satellite data are slightly
 530 overestimated compared to the surface data (bias -0.035 or 5.54% and -0.015 or -
 531 2.43%, respectively).

532 It is important to note that the agreement of satellite and surface data is better in
 533 spring and summer, for all studied wavelengths. Specifically, in case of MODIS-Aqua
 534 g_{aer} , the correlation coefficients increase up to 0.35, 0.50 and 0.54 at 440/470 nm,
 535 660/675 nm and 870 nm, respectively, while the bias decreases down to 0.0005
 536 (0.07%), 0.003 (0.46%) and 0.007 (1.11%), respectively.

537 Moreover, we find that for all seasons g_{aer} values at 870 nm and 660 nm, both from
538 MODIS-Terra and MODIS-Aqua, are overestimated compared to g_{aer} (AERONET) at the
539 corresponding wavelengths (stronger overestimation at 870 nm and by Terra). Finally
540 we note an underestimation of g_{aer} at 470 nm from MODIS-Aqua, relative to the data
541 by AERONET at 440 nm, while very small biases ($<0.5\%$) are found between Terra
542 and AERONET at the same wavelengths.

543 In Fig. 9 we present a scatterplot comparison between MODIS and AERONET g_{aer}
544 data pairs. There is bias towards larger g_{aer} values from both Aqua and Terra
545 compared to AERONET, with Terra overpredicting more than Aqua. The root mean
546 square error to the fit between MODIS and AERONET is very similar between Aqua
547 and Terra. There are concerns on the application of ordinary least squares regression,
548 arising from the assumption that as the assigned independent variable, AERONET
549 values should be free from error. We cannot guarantee the validity of this assumption,
550 so we recognize that the reported R and slope values from Fig. 9 and Table 1, if
551 viewed as metrics of agreement between MODIS g_{aer} and real g , may be subject to the
552 effect of regression dilution and consequently biased low. This possible bias for R and
553 slope could be neglected only if AERONET errors can also be considered negligible.
554 With the above caveat in mind, the applied least-squares fit line to the scatterplot
555 comparison between matched MODIS-AERONET data pairs (Fig. 9) indicates that
556 MODIS overestimates g_{aer} more in the smaller than larger values, i.e. more for fine
557 than coarse particles.

558 We present the frequency distributions of asymmetry parameter daily values (Fig. 10)
559 on the days when data from all three databases (MODIS-Terra, MODIS-Aqua and
560 AERONET) were provided. Fig. 10a corresponds to the whole area of interest, while
561 Figs. 10b and c correspond to two broad sub-regions with basic differences in the
562 aerosol source, namely Europe with great anthropogenic sources, and Africa, Middle
563 East and Arabian peninsula, with predominant natural sources and mainly desert dust.
564 There is an apparent skew in the MODIS-Terra and MODIS-Aqua g_{aer} distributions,
565 while the AERONET distributions are more symmetrical. Moreover, the satellite data
566 distributions show larger values and smaller standard deviations compared to
567 AERONET, with the Terra overestimation being more exaggerated. The disagreement
568 is more pronounced in the sub-region of Europe, while in the sub-region of North
569 Africa / Arabian peninsula, the distributions of satellite and surface data agree more
570 thus confirming the finding of Fig. 9 based on the slope of applied linear regression

571 fit. Values over Europe are generally smaller than over North Africa / Arabian
 572 peninsula (Fig. 3), which can be attributed to the presence of larger size particles of
 573 desert origin in the latter sub-region, in contrast to Europe, where due to industrial
 574 activity and frequent biomass burning the presence of smaller size particles is
 575 important. Therefore, the smaller g_{aer} values (<0.6) in the frequency distributions of
 576 the whole area, are overwhelmingly contributed by the European sub-region,
 577 contrasting with larger values (0.7-0.75) being contributed by both sub-regions and
 578 even more by N. Africa/Arabian peninsula at larger g_{aer} .

579 The overall comparison between satellite and surface g_{aer} data performed in the
 580 scatterplot of Fig. 9 and Table 1 does not allow one to have an insight to how the
 581 comparison behaves spatially, namely how it differs from one region to another. This
 582 is addressed in Fig. 11, showing the comparison of satellite and surface data at the
 583 wavelength of 870 nm separately between MODIS-Terra - AERONET and MODIS-
 584 Aqua – AERONET. For this comparison, we selected AERONET stations for which
 585 there is satisfactory overlap between the time series from AERONET and the time
 586 series from MODIS, namely the number of common days between AERONET-Terra
 587 and AERONET-Aqua is larger than 100. This criterion is satisfied by 36 stations for
 588 AERONET-Terra and by 34 for AERONET-Aqua shown in Fig. 11. For each
 589 AERONET station we compute the Pearson correlation coefficient between the
 590 station data and the corresponding MODIS-Terra or Aqua data at 870 nm, for the
 591 $1^{\circ} \times 1^{\circ}$ cell containing the station. Moreover, there is the information if the trends
 592 between AERONET and either MODIS-Terra or Aqua have the same sign (blue
 593 color) or not (red color).

594 In the case of the $g_{aer}(\text{AERONET}) - g_{aer}(\text{Terra})$ comparison, at 5 stations, (i.e. in 14% of
 595 total 36 stations), the correlation coefficient R is larger than 0.5 (largest R found is
 596 0.64 at station “Bahrain”), while at 13 stations (36 %) and 26 stations (72%) R is
 597 larger than 0.4 and 0.3, respectively. With respect to the agreement on the sign of the
 598 trends, at 24 out of 36 stations (67%) there is a trend sign match and at 12 stations
 599 (33%) a mismatch. Nevertheless, it should be noted that no systematic spatial
 600 behaviour, i.e. homogeneous spatial patterns, is found concerning the performance of
 601 MODIS-Terra g_{aer} against AERONET in terms of either the magnitude of correlation
 602 or the agreement of trends between the satellite and ground datasets. A similar picture
 603 emerges for the comparison $g_{aer}(\text{AERONET}) - g_{aer}(\text{Aqua})$. In this case, there are again 5
 604 stations (15% of total 34 stations) with $R > 0.5$ (maximum value $R = 0.61$ again at

605 “Bahrain”), while at 13 stations (38%) and 24 stations (71%) R is larger than 0.4 and
606 0.3, respectively. Also, we see that at 22 stations (65%) there is a trend sign match
607 and at 12 (35%) there is a mismatch.

608

609 **5 Summary and Conclusions**

610 Using satellite data from collection (051) of MODIS-Terra and Aqua data, we
611 examine the spatiotemporal variations of the aerosol asymmetry parameter (g_{aer}) over
612 North Africa, the Arabian peninsula and Europe. To our knowledge, this is the first
613 time that a satellite (MODIS) based dataset of g_{aer} , assessed and evaluated (against
614 AERONET data), is used for the study region. This is important, since such an
615 evaluated satellite dataset is very useful for many applications, like radiative transfer
616 and climate modelling as well as for remote sensing. The advantages of MODIS g_{aer}
617 data are that:

- 618 (i) They ensure complete spatial coverage over sea surfaces surrounding Europe,
619 Mediterranean and Middle East, which is essential for investigating and
620 understanding physical processes related to aerosols. These processes are
621 strongly dependent on the aerosol radiative and optical properties, g_{aer} being one
622 of the three key ones (the other two being aerosol optical thickness and single
623 scattering albedo). Such a complete spatial coverage is especially required by
624 radiative transfer and climate models.
- 625 (ii) They provide with spectral g_{aer} values, at 7 wavelengths from 470 to 2130 nm,
626 which are of essential importance for radiative transfer models. Such spectrally
627 resolved aerosol optical properties can induce significant differences in model
628 computations of aerosol radiative effects (Hatzianastassiou et al., 2007).
- 629 (iii) They provide a relatively long temporal coverage, i.e. 8 years, which is
630 significant for examining seasonal and inter-annual cycles and changes of this
631 aerosol optical property, especially combined with the complete spatial coverage.
632 This is also important since it provides a reasonable statistical bed for attempting
633 evaluations through comparison against other g_{aer} data like the AERONET.
- 634 (iv) They constitute the first to know so far satellite based g_{aer} dataset; until now, the
635 utilized g_{aer} data in modelling or other analyses were taken from in-situ
636 measurements or aerosol models, which both have their own deficiencies, namely
637 limited spatial coverage or pure theoretical basis.

638 According to the obtained results, generally, the largest values of the asymmetry
639 parameter, indicating the strongest forward scattering of radiation by atmospheric
640 aerosols, are found over areas with aerosol load being dominated by large size
641 particles of desert dust (tropical Atlantic, Arabian and Red Seas),. On the contrary,
642 smaller g_{aer} values are seen where a significant fraction of aerosol load comes from
643 small size particles of anthropogenic origin, e.g. over the Black Sea. The results are
644 consistent with the theory and thus prove a good performance of the MODIS retrieval
645 of aerosol asymmetry parameter. Depending on the area of interest, the seasonal cycle
646 of the asymmetry parameter varies markedly. More specifically, in areas with
647 abundance of desert dust particles, the range of intra-annual variation is small, with
648 the largest values during summer, while in other areas the seasonality is reversed, with
649 the largest values during the cold season and the smallest during the warm season.
650 The asymmetry parameter decreases with wavelength, especially when one examines
651 its spatially minimum values, while this decrease is weaker for the larger g_{aer} values,
652 corresponding to the presence of coarser particles.

653 The seasonal fluctuation is more pronounced with increasing wavelength in the
654 examined regions, which is attributed to the different spectral behaviour of the
655 asymmetry parameter for small and large particles. With respect to the inter-annual
656 variability of the asymmetry parameter, we did not discern very important either
657 increasing or decreasing tendencies, with absolute changes smaller than 0.04 in any
658 case. On the other hand, we found opposing tendencies for the two satellite datasets.
659 MODIS-Terra observes mostly increasing tendencies, while Aqua gives also a few
660 regions with decreasing tendencies. Generally, the largest intra-annual and inter-
661 annual variations are seen over the Black Sea, while the smallest over the tropical
662 Atlantic. However, some strong trends (especially from Terra) may be due to
663 calibration drift errors, which may be addressed in collection 006. Along these lines
664 we performed some preliminary comparisons between 051 and 006 Ångström
665 Exponent trends from Aqua, which ensured that AE and g_{aer} are very closely anti-
666 correlated. These preliminary results, show that 051 Aqua AE trends resemble very
667 closely the 006 trends, supporting that the g_{aer} trends from collection 051 (at least for
668 Aqua) reported in this study are credible.

669 The 051 MODIS g_{aer} data is not a retrieved but a derived MODIS parameter. Given
670 that the retrieval is strongly dependent on the assumptions made, namely on the
671 aerosol modes used, uncertainties can be associated with its use in radiative transfer
672 modeling. In order to examine these uncertainties, the g_{aer} data were compared with

673 051 AE data for the same period. The results from the comparison showed a strong
674 anti-correlation (coefficient higher than 0.7-0.8) proving the consistency and
675 reasonably safe use of g_{aer} data in modeling studies, at least to the same degree with
676 MODIS AE data in modeling and other analyses. The correlation is even higher over
677 sea areas characterized by stronger presence of fine aerosols, like the Black Sea, the
678 Persian Gulf or the North Sea. This confidence is further strengthened by the small
679 identified uncertainties related with the use of collection 051 instead of 006 MODIS
680 g_{aer} data reported in the previous paragraph. This was obtained indirectly based on the
681 use of AE data of both collections since g_{aer} data are not yet available in collection
682 006.

683 We compare satellite data with surface data from the AERONET, in order to further
684 validate the reliability of the former. Through the examination of frequency
685 distributions of daily g_{aer} , a shift of satellite data towards larger values relative to
686 surface data becomes apparent. This finding is more pronounced for g_{aer} over Europe,
687 while the North African, Arabian peninsula values are more in agreement. Moreover,
688 the smallest g_{aer} values originate from particles from Europe, because of the
689 generation of smaller size particles by industrial activities and biomass burning.

690 We present scatter plots of daily g_{aer} values between MODIS-Terra, MODIS-Aqua,
691 and AERONET, which show moderate agreement between satellite data at 470 nm
692 and surface data at 440 nm, with small correlation coefficients ($R < 0.3$) and a slight
693 underestimation by MODIS. Slightly better agreement was noted at larger
694 wavelengths, but still without reaching very satisfactory levels ($R < 0.47$).
695 Nevertheless, during spring and summer, satellite and surface measurements tend to
696 agree more. Finally, for the comparisons at 660/675 and 870 nm, we report an
697 overestimation of g_{aer} by MODIS compared to AERONET,.

698 When examined at the local scale, i.e. station by station, the MODIS g_{aer} data agree
699 reasonably and for some stations better than in overall, but still not very well, with
700 those of AERONET. This analysis, based on 36 and 34 AERONET stations ensuring
701 at least 100 common days with MODIS-Terra and Aqua, respectively, shows that in
702 36 and 38% of stations, respectively, the MODIS data have correlation coefficients
703 larger than 0.4 (reaching values up to 0.64), while in about 65% of stations the trends
704 of g_{aer} from MODIS and AERONET have the same sign. Nevertheless, the magnitude
705 of correlation coefficients or the agreement between trends of g_{aer} from the satellite
706 and ground datasets do not exhibit a systematic (homogeneous) spatial pattern.

707 Our results offer an interesting way to assess the uncertainty induced by the use of
708 such satellite g_{aer} data in climate and radiative transfer models that compute aerosol
709 radiative and climate effects. Based on an overall assessment of satellite MODIS g_{aer}
710 through detailed comparisons against ground AERONET data, it appears that in
711 overall MODIS performs satisfactorily in terms of magnitude of g_{aer} values. This is
712 indicated by the computed biases, which are smaller than 5% with respect to MODIS
713 values, with better performance at smaller wavelengths. The root mean squared errors
714 vary within the range 5-10% again being smaller for smaller wavelengths. These
715 results indicate an uncertainty of MODIS g_{aer} data over the study region up to of 10%
716 at maximum. Previous analyses and sensitivity studies for the same study region
717 (Papadimas et al., 2012) have shown that such g_{aer} uncertainties can induce
718 modifications of aerosol direct radiative effects (DREs) which are equal to 30% at the
719 top-of-atmosphere (TOA) and 1% in the atmosphere and 10% at the surface, at
720 maximum. Therefore, the uncertainty associated with the use of MODIS g_{aer} is larger
721 as to any aerosol related physical process taking place at TOA, namely planetary
722 cooling or warming and its magnitude, smaller for processes at the Earth's surface,
723 e.g. surface cooling and very small for aerosol processes and feedbacks in the
724 atmosphere, like the aerosol semi-direct effect and its implications. Results from the
725 same previous analysis (Papadimas et al., 2012) proved that the exact magnitude of
726 MODIS g_{aer} DRE uncertainty can be estimated by simple linear equations relating
727 DREs and g_{aer} , separately given for TOA, atmosphere and surface.

728 The results of the present analysis are useful since they assess for the first time the
729 performance of satellite based products of aerosol asymmetry parameter over broad
730 regions of special climatic interest. The obtained results are relatively satisfactory
731 given the difficulties encountered by satellite retrieval algorithms due to the different
732 assumptions they made. Nevertheless, our results and identified weaknesses remind
733 that users should be aware of the g_{aer} uncertainties and their consequences. The
734 identified weaknesses may provide an opportunity to improve such satellite retrievals
735 of aerosol asymmetry parameter in forthcoming data products like those of MODIS
736 C006. The increased temporal coverage of g_{aer} data, combined with the continued
737 operation of MODIS, is expected to make possible the building of the first real
738 satellite climatology of this important aerosol optical property.

739

740 **6 Acknowledgments**

741 This research has been co-financed by the European Union (European Social Fund –
742 ESF) and Greek national funds through the operational programme “Education and
743 Lifelong Learning” of the National Strategic Reference Framework (NSRF) –
744 Research Funding Program: THALES. Investing in knowledge society through the
745 European Social Fund. The Collection 051 MODIS-Terra data were obtained from
746 NASA’s Level 1 and Atmosphere Archive and Distribution System (LAADS) website
747 (<ftp://ladsweb.nascom.nasa.gov/>). We would like to thank the principal investigators
748 maintaining the AERONET sites used in the present work. We would also like to
749 thank three anonymous Reviewers and Dr Kaskaoutis for helping to improve the
750 manuscript with their comments.

751

752 **References**

- 753 Alonso-Pérez S., Cuevas E., Querol X., Guerra J. C., and Pérez C. (2012). African dust source
754 regions for observed dust outbreaks over the Subtropical Eastern North Atlantic region,
755 above 25°N, *J. Arid Environ.*, 79, 100-109, [doi:10.1016/j.jaridenv.2011.11.013](https://doi.org/10.1016/j.jaridenv.2011.11.013).
- 756 Barnaba F. and G. P. Gobbi: Aerosol seasonal variability over the Mediterranean region and
757 relative impact of maritime, continental and Saharan dust particles over the basin from
758 MODIS data in the year 2001, *Atmospheric Chemistry and Physics*, 4, 4285 - 4337, SRef-
759 ID: 1680-7375/acpd/2004-4-4285 SRef-ID: 1680-7375/acpd/2004-4-4285, 2004.
- 760 Barnaba F., Angelini F., Curci G., and Gobbi G. P. (2011), An important fingerprint of
761 wildfires on the European aerosol load, *Atmos. Chem. Phys.*, 11, 10,487–10,501.
- 762 Bovchaliuk A., Milinevsky G., Danylevsky V., Goloub P., Dubovik O., Holdak A., and
763 Sosonkin, M. (2013). Variability of aerosol properties over Eastern Europe observed from
764 ground and satellites in the period from 2003 to 2011. *Atmos. Chem. Phys.*, 13, 6587-6602
- 765 Bréon F.-M., Vermeulen A., and Descloitres J. (2011). An evaluation of satellite aerosol
766 products against sunphotometers measurements, *Remote Sens. Environ.*, 115, 3102–3111.
- 767 Chubarova, N. Y.: Seasonal distribution of aerosol properties over Europe and their impact on
768 UV irradiance, *Atmos. Meas. Tech.*, 2, 593–608, doi:10.5194/amt-2-593-2009, 2009.
- 769 Di Iorio, T., A. di Sarra, W. Junkermann, M. Cacciani, G. Fiocco, and D. Fua, Tropospheric
770 aerosols in the Mediterranean: 1. Microphysical and optical properties, *J. Geophys. Res.*,
771 108(D10), 4316, doi:10.1029/2002JD002815, 2003
- 772 Dubovik, Oleg, Brent Holben, Thomas F. Eck, Alexander Smirnov, Yoram J. Kaufman,
773 Michael D. King, Didier Tanré, Ilya Slutsker, 2002: Variability of Absorption and Optical
774 Properties of Key Aerosol Types Observed in Worldwide Locations. *J. Atmos. Sci.*, **59**,
775 590–608.
- 776 Dubovik, O. and M. D. King, 2000: A flexible inversion algorithm for retrieval of aerosol
777 optical properties from Sun and sky radiance measurements," *J. Geophys. Res.*, 105, 20
778 673-20 696.
- 779 Engelstaedter S., Tegen I., and Washington R. (2006). North African dust emissions and
780 transport, *Earth-Sci. Revi.*, 79(1-2), 73-100.
- 781 Fotiadi, A., E. Drakakis, N. Hatzianastassiou, C. Matsoukas, K. G. Pavlakis, D.
782 Hatzidimitriou, E. Gerasopoulos, N. Mihalopoulos, and I. Vardavas (2006), Aerosol
783 physical and optical properties in the eastern Mediterranean Basin, Crete, from Aerosol
784 Robotic Network data, *Atmos. Chem. Phys.*, 6, 5399– 5413.
- 785 Gerasopoulos, E., Kouvarakis, G., Babasakalis, P., Vrekoussis, M., Putaud, J. P., and
786 Mihalopoulos, N.: Origin and variability of particulate matter (PM10) mass concentrations
787 over the Eastern Mediterranean, *Atmos. Environ.*, 40, 4679–4690, 2006.

- 788 Ginoux P, Prospero J. M., Gill T. E., Hsu C. N., Zhao M., (2012). Global-scale attribution of
789 anthropogenic and natural dust sources and their emission rates based on MODIS Deep
790 Blue aerosol products. *Rev. Geophys.* 50, RG3005. doi:10.1029/2012RG000388.
- 791 Gkikas, A., Hatzianastassiou, N., and Mihalopoulos, N.: Study and characterization of aerosol
792 episodes in the Mediterranean basin for the 7-year period 2000–2007 based on MODIS
793 data, European Aerosol Conference, Greece, Thessaloniki, 24–29 August 2008.
- 794 Gkikas, A., Hatzianastassiou, N., and Mihalopoulos, N.: Aerosol events in the broader
795 Mediterranean basin based on 7-year (2000–2007) MODIS C005 data, *Ann. Geophys.*, 27,
796 3509–3522, doi:10.5194/angeo-27-3509-2009, 2009.
- 797 Gkikas, A., Houssos, E., Hatzianastassiou, N., Papadimas, C. and Bartzokas, A. (2011),
798 Synoptic conditions favouring the occurrence of aerosol episodes over the broader
799 Mediterranean basin. *Q.J.R. Meteorol. Soc.* doi: 10.1002/qj.978.
- 800 Gkikas, A., Hatzianastassiou, N., Mihalopoulos, N., Katsoulis, V., Kazadzis, S., Pey, J., and
801 Torres, O. (2013). The regime of intense desert dust episodes in the Mediterranean based
802 on contemporary satellite observations and ground measurements. *Atmos. Chem. Phys.*,
803 13, 12135-12154.
- 804 Gkikas A., Houssos E. E., Lolis C. J., Bartzokas A., Mihalopoulos N., and Hatzianastassiou
805 N. (2014), Atmospheric circulation evolution related to desert-dust episodes over the
806 Mediterranean. *Quart. J. Roy. Meteorol. Soc.*, 690, 1634-1645.
- 807 Goloub, P., and O. Arino, 2000: Verification of the consistency of POLDER aerosol index
808 over land with ATSR-2 fire product. *Geophys. Res. Lett.*, 27, 899–902.
- 809 Graßl, H.: Possible changes of planetary albedo due to aerosol particles, in *Man's Impact on*
810 *Climate*, edited by: W. Bach, J. Pankrath, and W. Kellogg, Elsevier, New York, 1979.
- 811 Hansen, J., Sato, M., and Ruedy, R.: Radiative forcing and climate response, *J. Geophys.*
812 *Res.*, 102, 6831–6864, 1997.
- 813 Hatzianastassiou, N., B. Katsoulis, I. Vardavas: Sensitivity analysis of aerosol direct radiative
814 forcing in ultraviolet - visible wavelengths and consequences for the heat budget, *Tellus*,
815 56b, 368 - 381, 2004.
- 816 Hatzianastassiou, N., A. Gkikas, N. Mihalopoulos, O. Torres, and B. D. Katsoulis: Natural
817 versus anthropogenic aerosols in the eastern Mediterranean basin derived from multiyear
818 TOMS and MODIS satellite data, *J. Geophys. Res.*, 114, D24202,
819 doi:10.1029/2009JD011982, 2009.
- 820 Hatzianastassiou, N., Matsoukas, C., Drakakis, E., Stackhouse Jr., P. W., Koepke, P.,
821 Fotiadi, A., Pavlakis, K. G., and Vardavas, I.: The direct effect of aerosols on solar
822 radiation based on satellite observations, reanalysis datasets, and spectral aerosol optical
823 properties from Global Aerosol Data Set (GADS), *Atmos. Chem. Phys.*, 7, 2585-2599,
824 doi:10.5194/acp-7-2585-2007, 2007.

- 825 Haywood, J.M., and O. Boucher, 2000: Estimates of the direct and indirect radiative forcing
826 due to tropospheric aerosols: A review. *Rev. Geophys.*, 38, 513–543.
- 827 Heishman, J. (1999), Commanding Officer, Forecaster's Handbook, U.S. Navy Cent.
828 Meteorol. and Oceanogr. Cent., Manama, Bahrain.
- 829 Holben B.N., T.F. Eck, I. Slutsker, D. Tanré, J.P. Buis, A. Setzer, E. Vermote, J.A. Reagan,
830 Y. Kaufman, T. Nakajima, F. Lavenu, I. Jankowiak, and A. Smirnov, 1998: AERONET -
831 A federated instrument network and data archive for aerosol characterization, *Rem. Sens.*
832 *Environ.*, 66, 1-16.
- 833 Ichoku C., D. Allen Chu, Shana Mattoo, Yoram J. Kaufman, Lorraine A. Remer, Didier Tanré,
834 Ilya Slutsker, and Brent N. Holben: A spatio-temporal approach for global validation and
835 analysis of MODIS aerosol products. *GEOPHYSICAL RESEARCH LETTERS*, VOL. 29,
836 NO. 12, 10.1029/2001GL013206, 2002.
- 837 IPCC, 2007: *Climate Change 2007: The Physical Science Basis*. Contribution of Working
838 Group I to the Fourth Assessment Report of the Intergovernmental Panel on Climate
839 Change [Solomon, S., D. Qin, M. Manning, Z. Chen, M. Marquis, K.B. Averyt, M. Tignor
840 and H.L. Miller (eds.)]. Cambridge University Press, Cambridge, United Kingdom and
841 New York, NY, USA.
- 842 IPCC, 2013: *Climate Change 2013: The Physical Science Basis*. Contribution of Working
843 Group I to the Fifth Assessment Report of the Intergovernmental Panel on Climate Change
844 [Stocker, T.F., D. Qin, G.-K. Plattner, M. Tignor, S.K. Allen, J. Boschung, A. Nauels, Y.
845 Xia, V. Bex and P.M. Midgley (eds.)]. Cambridge University Press, Cambridge, United
846 Kingdom and New York, NY, USA, 1535 pp.
- 847 Joseph J. H., Wiscombe W. J., and Weinman, J. A. (1976). The delta-Eddington
848 approximation for radiative flux transfer. *J. Atmos. Sci.*, 33, 2452–2459.
- 849 Jianrong Bi, Jianping Huang, Qiang Fu, XinWanga, Jinsen Shi, Wu Zhang, Zhongwei
850 Huang, Beidou Zhang: Toward characterization of the aerosol optical properties over
851 Loess Plateau of Northwestern China. *Journal of Quantitative Spectroscopy & Radiative*
852 *Transfer* 112 (2011) 346–360.
- 853 Kalapureddy, M. C. R., D. G. Kaskaoutis, P. Ernest Raj, P. C. S. Devara, H. D. Kambezidis,
854 P. G. Kosmopoulos, and P. T. Nastos (2009), Identification of aerosol type over the
855 Arabian Sea in the premonsoon season during the Integrated Campaign for Aerosols,
856 Gases and Radiation Budget (ICARB), *J. Geophys. Res.*, 114, D17203,
857 doi:10.1029/2009JD011826.
- 858 Kalivitis, N., Gerasopoulos, E., Vrekoussis, M., Kouvarakis, G., Kubilay, N.,
859 Hatzianastassiou, N., Vardavas, I., and Mihalopoulos, N.: Dust transport over the eastern
860 Mediterranean derived from TOMS, AERONET and surface measurements, *J. Geophys.*
861 *Res.*, 112, D03202, doi:10.1029/2006JD007510, 2007.

- 862 Kaufman, Y. J., D. Tanré, L. A. Remer, E. F. Vermote, A. Chu, and B. N. Holben:
863 Operational remote sensing of tropospheric aerosol over land from EOS moderate
864 resolution imaging spectroradiometer, *J. Geophys. Res.*, 102, 17,051– 17,067, 1997.
- 865 Kinne, S., D. O'Donnell, P. Stier, S. Kloster, K. Zhang, H. Schmidt, S. Rast, M. Giorgetta, T.
866 F. Eck, and B. Stevens (2013), MAC-v1: A new global aerosol climatology for climate
867 studies, *J. Adv. Model. Earth Syst.*, 5, 704–740, doi:10.1002/jame.20035.
- 868 Kishcha, P., A. M. da Silva, B. Starobinets, C. N. Long, O. Kalashnikova, and P. Alpert,
869 Meridional distribution of aerosol optical thickness over the tropical Atlantic Ocean,
870 *Atmos. Chem. Phys. Discuss.*, 14, 23309-23339, 2014.
- 871 Koepke, P., M. Hess, I. Schult, and E. P. Shettle: Global aerosol data set, Rep. No. 243, Max-
872 Planck Institut fuer Meteorologie, Hamburg, Germany, 44 pp., 1997.
- 873 Kondratyev, K. Y. 1999. Climatic effects of aerosols and clouds. Springer, New York.
- 874 Kutiel H., Furman, H., (2003). Dust storms in the Middle East: sources of origin and their
875 temporal characteristics. *Indoor Built Environ.* 12, 419–426.
- 876 Lelieveld, J., et al. (2002), Global air pollution crossroads over the Mediterranean, *Science*,
877 298, 794– 799, doi:10.1126/science.1075457.
- 878 Levy, R. C., Remer, L. A., Kleidman, R. G., Mattoo, S., Ichoku, C., Kahn, R., and Eck, T. F.:
879 Global evaluation of the Collection 5 MODIS dark-target aerosol products over land,
880 *Atmos. Chem. Phys.*, 10, 10399-10420, doi:10.5194/acp-10-10399-2010, 2010.
- 881 Lohmann U., Feichter, J. [2005] Global indirect aerosol effects: A review . *Atmos. Chem.*
882 *Phys.*, 5, 715-737.
- 883 Miller S. D., Kuciauskas A. P., Liu M., Ji Q., Reid J. S., Breed D. W. Walker A. L., and
884 Mandoos A. A.. (2008). Haboob dust storms of the southern Arabian Peninsula, *J.*
885 *Geophys. Res.*, 113, D01202, doi:[10.1029/2007JD008550](https://doi.org/10.1029/2007JD008550).
- 886 Nabat P., Somot S., Malle, M., Chiapello I., Morcrette J. J., Solmon F., Szopa S., Dulac F.,
887 Collins W., Ghan S., Horowitz L. W., Lamarque J. F., Lee Y. H., Naik V., Nagashima T.,
888 Shindell D., and Skeie R. (2013), A 4-D climatology (1979–2009) of the monthly
889 tropospheric aerosol optical depth distribution over the Mediterranean region from a
890 comparative evaluation and blending of remote sensing and model products. *Atmos. Meas.*
891 *Tech.*, 6, 1287–1314.
- 892 Lyamani, H., F. J. Olmo, A. Alca'ntara, and L. Alados-Arboledas (2006), Atmospheric
893 aerosols during the 2003 heat wave in southeastern Spain. I: Spectral optical depth, *Atmos.*
894 *Environ.*, 40, 6453 – 6464, doi:10.1016/j.atmosenv.2006.04.048.
- 895 Papadimas, C. D., N. Hatzianastassiou, N. Mihalopoulos, X. Querol, and I.
896 Vardavas (2008), Spatial and temporal variability in aerosol properties over the
897 Mediterranean basin based on 6-year (2000–2006) MODIS data, *J. Geophys. Res.*, 113,
898 D11205, doi:10.1029/2007JD009189.

- 899 Papadimas C. D., Hatzianastassiou N., Matsoukas C., Kanakidou M., Mihalopoulos N., and
900 Vardavas, I. (2012). The direct effect of aerosols on solar radiation over the broader
901 Mediterranean basin. *Atmos. Chem. Phys.*, 12, 7165-7185.
- 902 Pace, G., A. di Sarra, Meloni, D., Piacentino, S., and Chamard, P.: Aerosol optical properties
903 at Lampedusa (Central Mediterranean). 1. Influence of transport and identification of
904 different aerosol types, *Atmos. Chem. Phys.*, 6, 697–713, 2006, [www.atmos-chem-](http://www.atmos-chem-phys.net/6/697/2006/)
905 [phys.net/6/697/2006/](http://www.atmos-chem-phys.net/6/697/2006/).
- 906 Pilinis, Ch., Pandis, S. N. and Seinfeld, J. H. 1996. Sensitivity of direct climate forcing by
907 anthropogenic aerosols to aerosol size distribution and composition. *J. Geophys. Res.* 100,
908 18 739–18 754.
- 909 Prospero, J., P. Ginoux, O. Torres, and S. E. Nicholson (2002), Environmental
910 Characterization of Global sources of atmospheric soil dust derived from the NIMBUS-7
911 TOMS absorbing aerosol product, *Rev. Geophys.*, 40(1), 1002,
912 doi:10.1029/20000GR000095.
- 913 Rahul, PRC and Salvekar, PS and Devara, PCS (2008) Aerosol optical depth variability over
914 Arabian Sea during drought and normal years of Indian monsoon. *Geophysical Research*
915 *Letters*, 35 (22).
- 916 Rashki A., Kaskaoutis D. G., de W. Rautenbach C. J., Eriksson P. G., Qiang M, and Gupta
917 P., (2012). Dust storms and their horizontal dust loading in the Sistan region, Iran. *Aeolian*
918 *Res* 5: 51–62.
- 919 Rashki A., Kaskaoutis D. G., Eriksson P. G., de W. Rautenbach C. J., Flamant C., Abdi
920 Vishkaee F., (2014). Spatio-temporal variability of dust aerosols over the Sistan region in
921 Iran based on satellite observations. *Nat. Hazards*, doi: 10.1007/s11069-013-0927-0.
- 922 Remer L.A., Tanre D., Kaufman Y.J., Levy R, and Matoo S.: Algorithm for Remote Sensing
923 of Tropospheric Aerosol from MODIS: Collection 005, 2006,
924 http://modis.gsfc.nasa.gov/data/atbd/atbd_mod02.pdf.
- 925 Remer L.A., Kaufman Y.J., Tanre D. and co-authors: The MODIS aerosol algorithm,
926 products, and validation, *J. Atmos. Sci.*, 62: 947-973, 2005.
- 927 Remer LA, Kleidman RG, Levy RC, Kaufman YJ, Tanre D, Mattoo S, Martins JV, Ichoku
928 C, Koren I, Yu H, Holben BN. 2008. Global aerosol climatology from the MODIS satellite
929 sensors. *Journal of Geophysical Research* 113: D14S07, DOI: 10.1029/2007JD009661.
- 930 Satheesh, S. K., V. Ramanathan, X. Li-Jones, J. M. Lobert, I. A. Podgorny, J. M. Prospero, B.
931 N. Holben, and N. G. Loeb, A model for the natural and anthropogenic aerosols over the
932 tropical Indian Ocean derived from Indian Ocean Experiment data, *J. Geophys. Res.*, 104,
933 27,421–27,440, 1999.
- 934 Satheesh, S. K., K. Krishna Moorthy, Y. J. Kaufman, and T. Takemura, Aerosol optical depth,
935 physical properties and radiative forcing over the Arabian Sea, *Meteorology and*
936 *Atmospheric Physics*, Volume 91, Issue 1, pp 45-62, 2006.

- 937 Savoie, D. L., J. M. Prospero, and R. T. Nees, Nitrate, nonsea-salt sulfate, and mineral
938 aerosol over the northwestern Indian Ocean, *J. Geophys. Res.*, 92, 933–942, 1987.
- 939 Sciare, J., H. Bardouki, C. Moulin, and N. Mihalopoulos (2003), Aerosol sources and their
940 contribution to the chemical composition of aerosols in the Eastern Mediterranean Sea
941 during summertime, *Atmos. Chem. Phys.*, 3, 291–302, SRef-ID:1680 – 7324/acp/2003–3-
942 291.
- 943 Smirnov A., Holben B. N., Dubovik O., O'Neill N. T., Eck T. F., Westphal D. L., Goroch A.
944 K., Pietras C., and Slutsker I, 2002a: Atmospheric Aerosol Optical Properties in the
945 Persian Gulf. *J. Atmos. Sci.*, **59**, 620–634, doi: [http://dx.doi.org/10.1175/1520-
946 0469\(2002\)059<0620:AAOPIT>2.0.CO;2](http://dx.doi.org/10.1175/1520-0469(2002)059<0620:AAOPIT>2.0.CO;2).
- 947 Smirnov, A., B. N. Holben, Y. J. Kaufman, O. Dubovik, T. F. Eck, I. Slutsker, C. Pietras, and
948 R. N. Halthore, 2002b: Optical properties of atmospheric aerosol in maritime
949 environments. *J. Atmos. Sci.*, **59**, 501–523.
- 950 Smirnov, A., B. N. Holben, T. F. Eck, I. Slutsker, B. Chatenet, and R. T. Pinker, 2002c:
951 Diurnal variability of aerosol optical depth observed at AERONET (Aerosol Robotic
952 Network) sites, *Geophys. Res. Lett.*, **29**, 23, 2115, doi:10.1029/2002GL016305.
- 953 Tanré, D., Y. J. Kaufman, M. Herman, and S. Mattoo: Remote sensing of aerosol properties
954 over oceans using the MODIS/EOS spectral radiances, *J. Geophys. Res.*, 102, 16,971–
955 16,988, 1997.
- 956 Tindale, N. W., and P. P. Pease, Aerosols over the Arabian Sea: Atmospheric transport
957 pathways and concentrations of dust and sea salt, *Deep Sea Res.*, 46, 1577–1595, 1999.
- 958 Yu, H., Dickinson, R. E., Chin, M., Kaufman, Y. J., Holben, B. N. Geogdzhayev, I. V., and
959 Mishchenko, M. I.: Annual cycle of global distributions of aerosol optical depth from
960 integration of MODIS retrievals and GOCART model simulations, *J. Geophys. Res.*, 108,
961 4128, doi:10.1029/2002JD002717, 2003.
- 962 Zdun, A., A. Rozwadowska and S. Kratzer, 2011. Seasonal variability in the optical
963 properties of Baltic aerosols, *Oceanologia*, 53(1), 7-34.
- 964 Zuluaga, M. D., P. J. Webster, and C. D. Hoyos (2012), Variability of aerosols in the tropical
965 Atlantic Ocean relative to African Easterly Waves and their relationship with atmospheric
966 and oceanic environments, *J. Geophys. Res.*, 117, D16207, doi:10.1029/2011JD017181.
- 967

968 **Table 1.** Correlation coefficients (R), mean bias, root mean squared error (RMSE)
 969 and the slope and intercept values of applied linear regression fits between MODIS
 970 and AERONET g_{aer} data. The statistical parameters are given separately for the pairs
 971 of wavelengths: (i) 470 nm (MODIS) and 440 nm (AERONET), (ii) 660 nm
 972 (MODIS) and 675nm (AERONET) and (iii) 870 nm (MODIS and AERONET). The
 973 statistical parameters are also given separately for winter, spring, summer and
 974 autumn. ^a

975

976 *MODIS-Terra*

977

		R	Bias*	RMSE	Slope	Intercept
year	470-440	0.25	2×10^{-4}	0.045	0.36	0.45
	660-675	0.41	-0.028	0.060	0.55	0.32
	870	0.47	-0.035	0.070	0.60	0.29
W i n t e r	470-440	0.20	4.5×10^{-4}	0.046	0.26	0.53
	660-675	0.35	-0.033	0.056	0.41	0.42
	870	0.41	-0.053	0.057	0.40	0.43
Sp r i n g	470-440	0.27	-5×10^{-4}	0.046	0.40	0.43
	660-675	0.44	-0.023	0.060	0.63	0.27
	870	0.50	-0.026	0.071	0.67	0.24
Su m m e	470-440	0.33	-0.002	0.044	0.51	0.35
	660-675	0.48	-0.031	0.061	0.71	0.22
	870	0.54	-0.030	0.077	0.79	0.16
Au t u m n	470-440	0.21	0.003	0.044	0.30	0.50
	660-675	0.33	-0.027	0.059	0.45	0.38
	870	0.41	-0.035	0.068	0.53	0.34

978

979

980 *MODIS-Aqua*

981

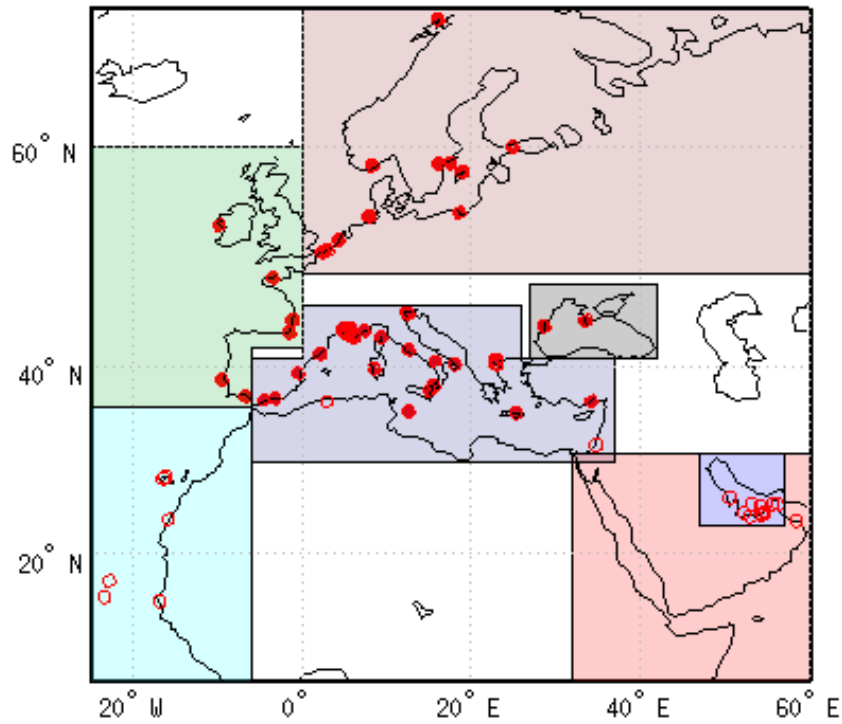
		R	Bias*	RMSE	Slope	Intercept
	470-440	0.27	0.018	0.047	0.41	0.40
	660-675	0.42	-0.005	0.062	0.61	0.26
	870	0.46	-0.015	0.072	0.61	0.26
W						

^aThe reported correlation coefficients and slopes may be biased low, because we did not include in our analysis the unknown AERONET errors.

i n t e r	470-440	0.25	0.024	0.049	0.36	0.43
	660-675	0.39	-0.001	0.062	0.55	0.30
	870	0.43	-0.021	0.068	0.51	0.33
Sp rin g	470-440	0.29	0.015	0.048	0.45	0.38
	660-675	0.45	-0.003	0.064	0.70	0.20
	870	0.50	-0.007	0.076	0.71	0.19
Su m me	470-440	0.35	0.014	0.045	0.55	0.30
	660-675	0.50	-0.012	0.060	0.72	0.19
	870	0.53	-0.018	0.074	0.73	0.19
Au t u m n	470-440	0.20	0.021	0.047	0.30	0.47
	660-675	0.32	-0.003	0.061	0.46	0.36
	870	0.37	-0.014	0.069	0.48	0.34

982
983
984

* $g_{aer}(AERONET) - g_{aer}(MODIS)$



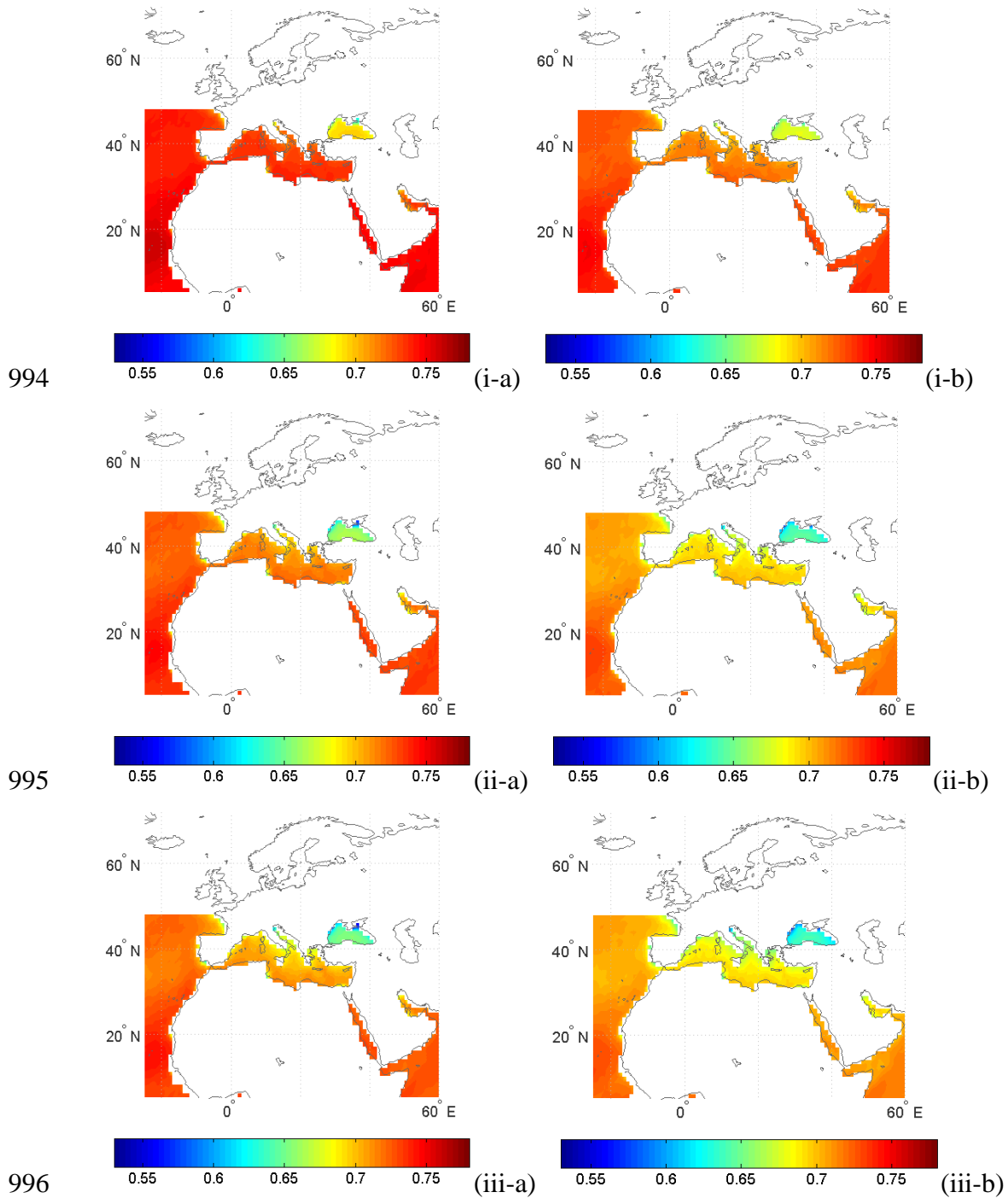
985

986

987 **Figure 1.** The study region (5°N–70°N, 25°W–60°E) and the location of 69
 988 AERONET stations used for validation of MODIS satellite aerosol asymmetry
 989 parameter (g_{aer}) data. Solid red circles denote stations located in Europe and hollow
 990 red circles are stations in Africa, Middle East and the Arabian peninsula. Also shown
 991 are seven sub-regions selected for studying the seasonal variation of g_{aer} .

992

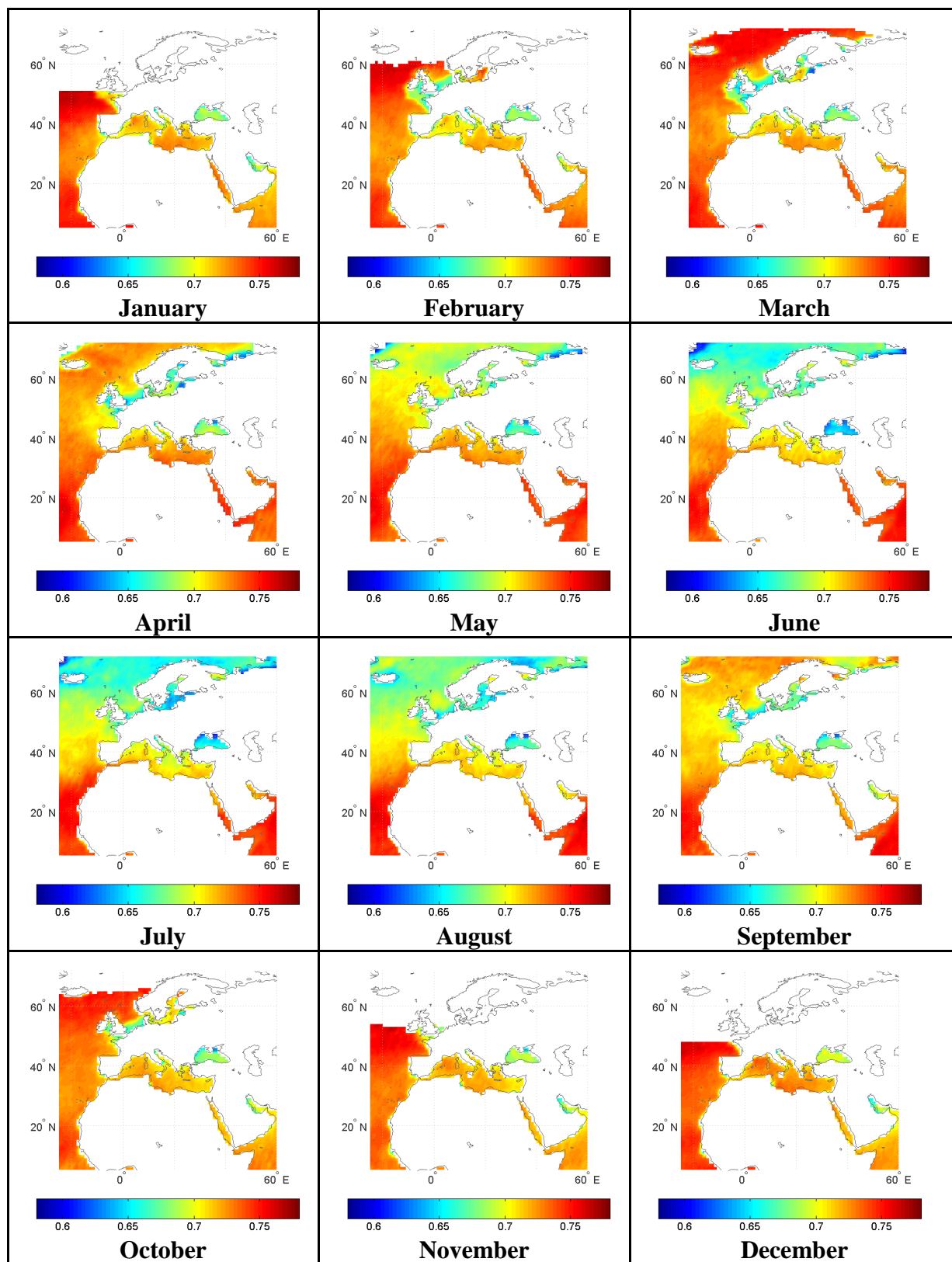
993



997

998 **Figure 2.** Geographical distribution of MODIS-Terra (-a, left column) and MODIS-
 999 Aqua (-b, right column) g_{aer} values averaged over 2002-2010, at the wavelengths of:
 1000 470 nm (i-, top row), 660 nm (ii-, middle row) and 860 nm (iii-, bottom row).

1001

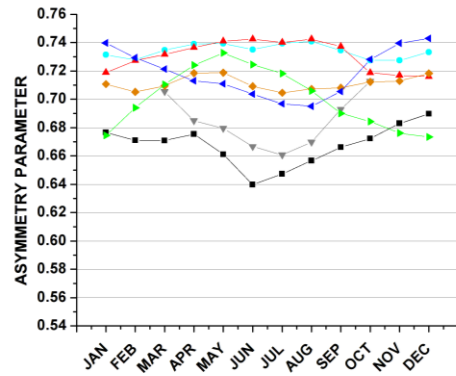
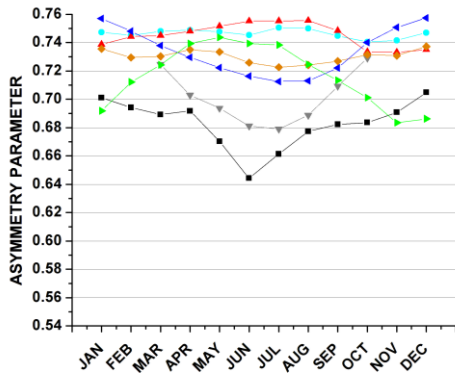


1003

1004 **Figure 3.** Month by month variation of MODIS-Aqua g_{aer} values at 470 nm averaged

1005 over the period 2002-2010.

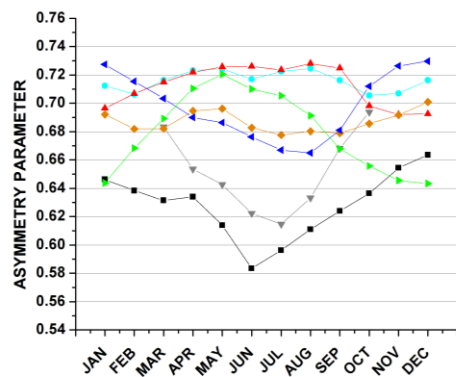
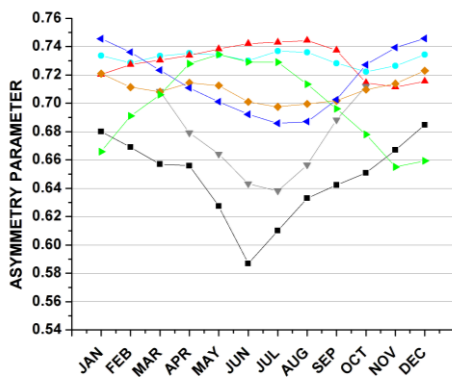
1006



1007

(i-a)

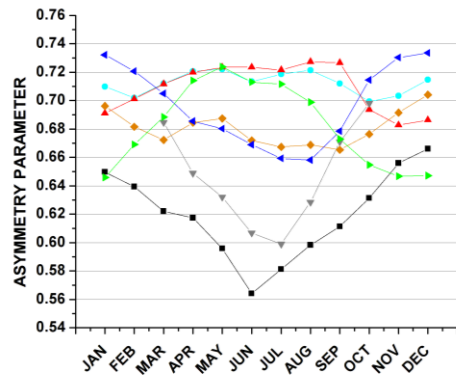
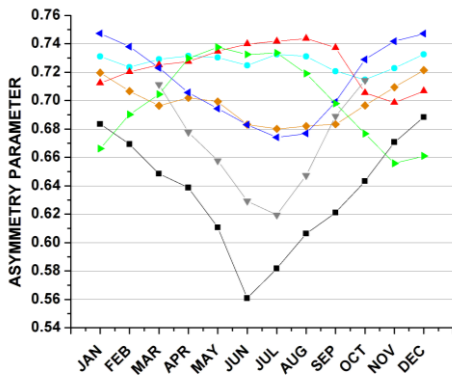
(i-b)



1008

(ii-a)

(ii-b)



1009

(iii-a)

(iii-b)



1010

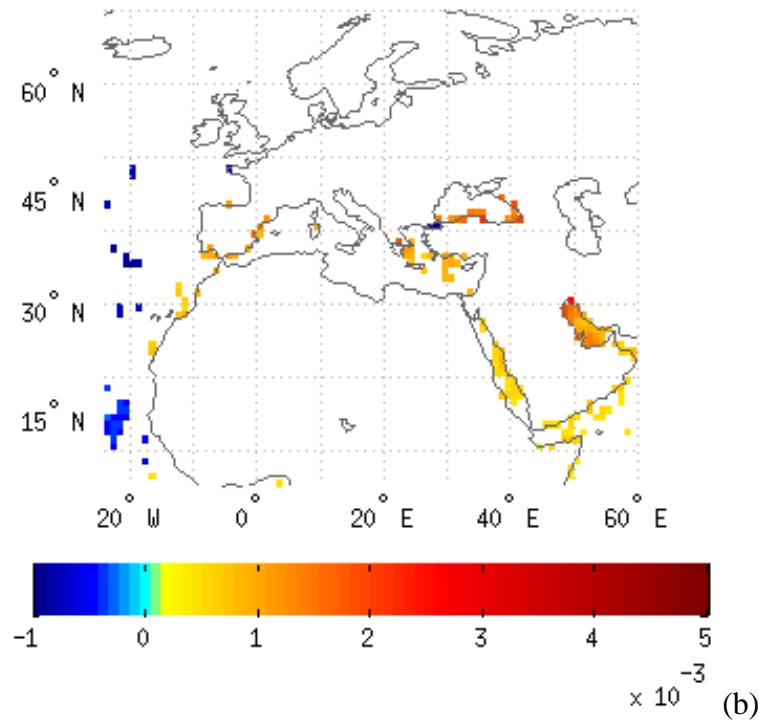
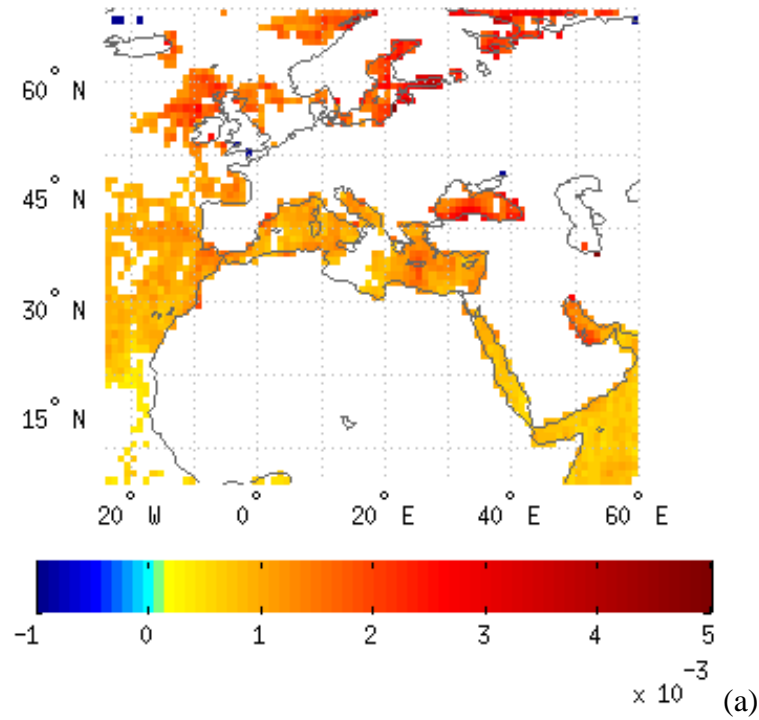
1011 **Figure 4.** Intra-annual variation of MODIS Terra (-a, left column) and Aqua (-b, right column)

1012 g_{aer} values averaged over seven selected sub-regions (Fig. 1). Results are

1013 given for g_{aer} values at: 470 nm (i-, top row), 660 nm (ii-, middle row) and 860 nm

1014 (iii-, bottom row), averaged over the period 2002-2010, respectively.

1015

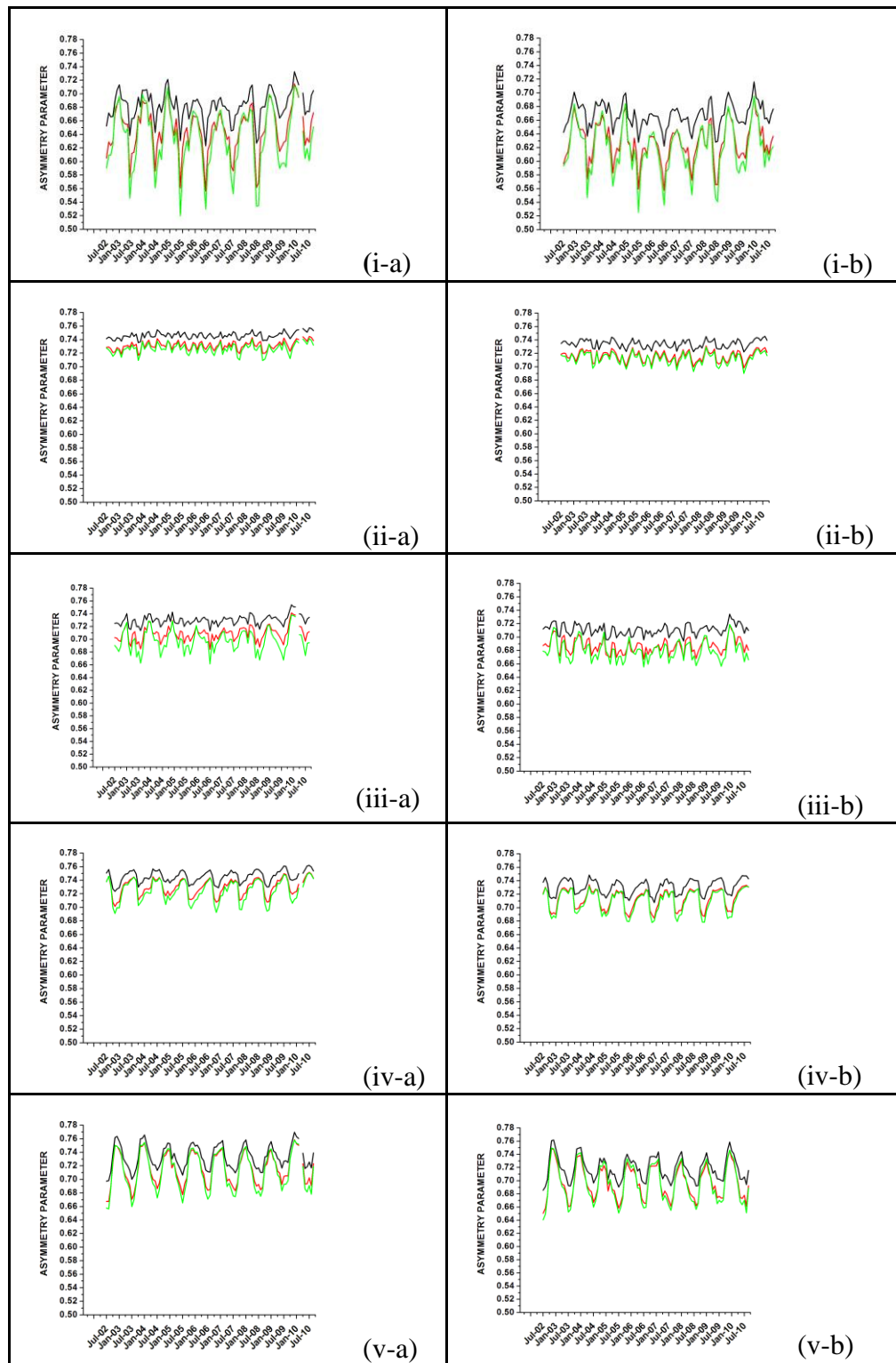


1017

1018

1019 **Figure 5.** Slope (in units decade⁻¹) of MODIS g_{aer} deseasonalized anomalies over the
 1020 period 2002-2010 from MODIS-Terra (-a, top) and MODIS-Aqua (-b, bottom), for
 1021 the wavelengths of 470 nm. Results are shown only if the trend is statistically
 1022 significant at the 95% confidence level.

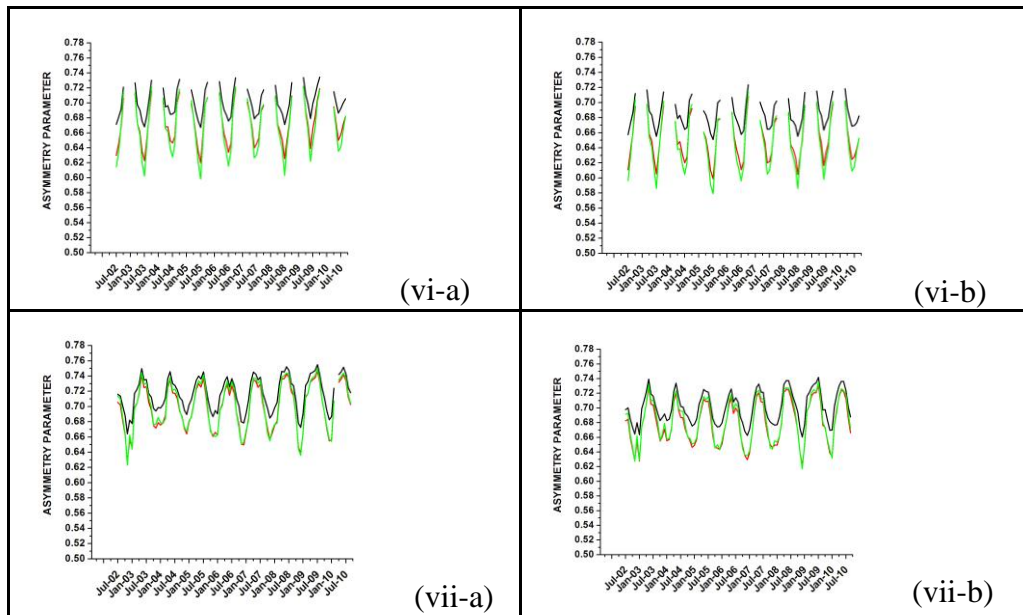
1023



1024

1025 **Figure 6.** Inter-annual (2002-2010) variation of monthly mean g_{aer} values at 470 nm
 1026 averaged over the sub-regions of: (i) Black Sea, (ii) Eastern Atlantic Ocean, (iii)
 1027 Mediterranean Sea, (iv) Middle East, (v) North-eastern Atlantic Ocean, (vi) North
 1028 Europe and (vii) Persian Gulf. Results are given based on MODIS-Terra (-a, left
 1029 column) and MODIS-Aqua (-b, right column).

1030

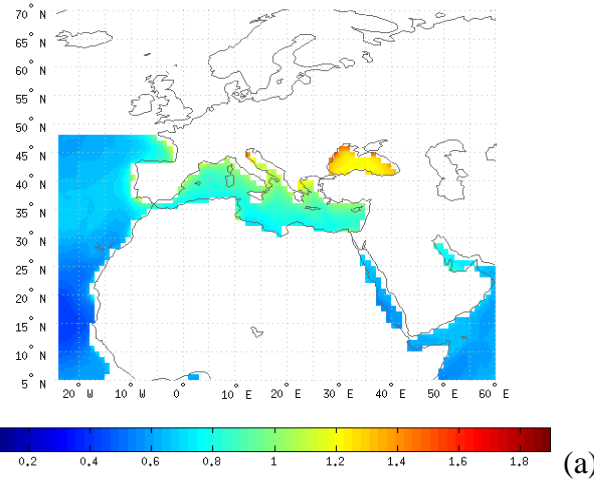


1031

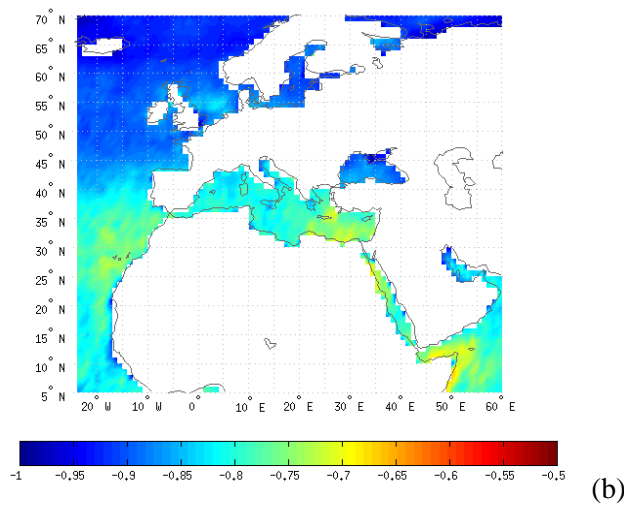
1032 **Figure 6 (continued).** Inter-annual (2002-2010) variation of monthly mean g_{aer} values
1033 at 470 nm averaged over the sub-regions of: (i) Black Sea, (ii) Eastern Atlantic Ocean,
1034 (iii) Mediterranean Sea, (iv) Middle East, (v) North-eastern Atlantic Ocean, (vi) North
1035 Europe and (vii) Persian Gulf. Results are given based on MODIS-Terra (-a, left
1036 column) and MODIS-Aqua (-b, right column).

1037

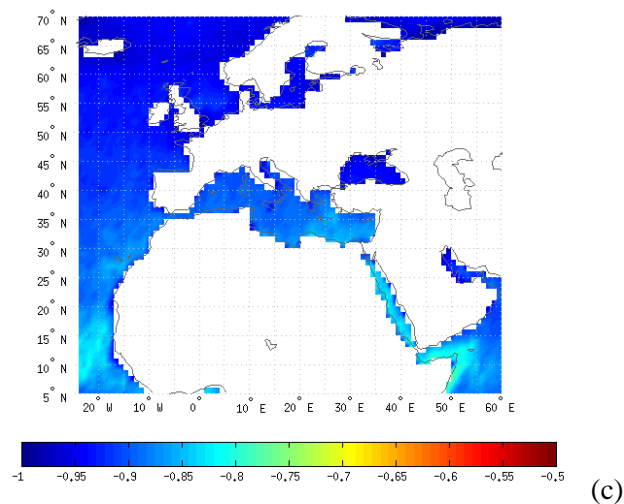
1038



1039

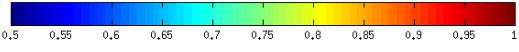
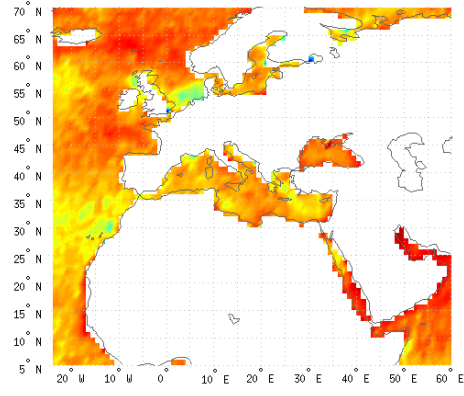
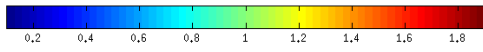
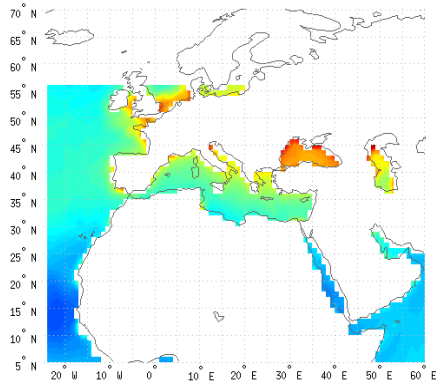


1040



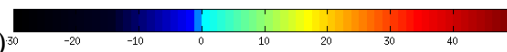
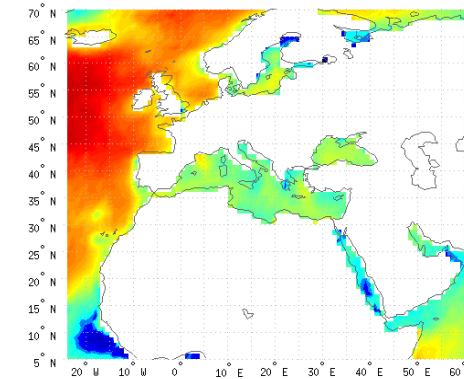
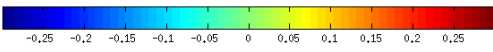
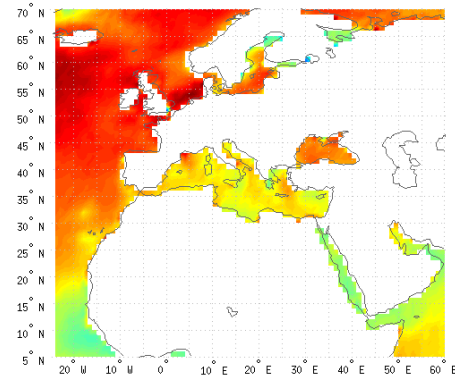
1041

1042 **Figure 7.** (a) Geographical distribution of MODIS-Aqua 051 Ångström exponent
 1043 ($AE_{550-865}$) values averaged over 2002-2010, at the wavelength pair of 550-865nm.
 1044 Winter AE data are missing from the northernmost areas and therefore the long-term
 1045 averages in (a) are left blank. The correlation coefficients between $AE_{550-865}$ and g_{aer}
 1046 data at 660 and 860 nm are given in (b) and (c), respectively.



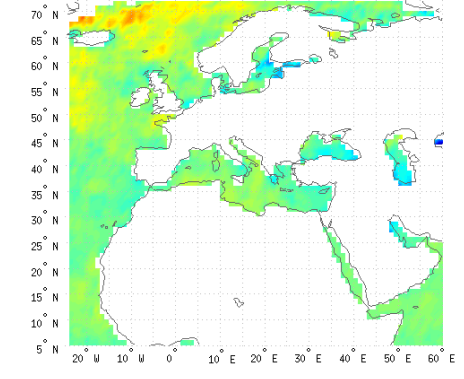
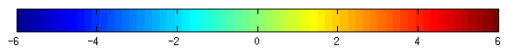
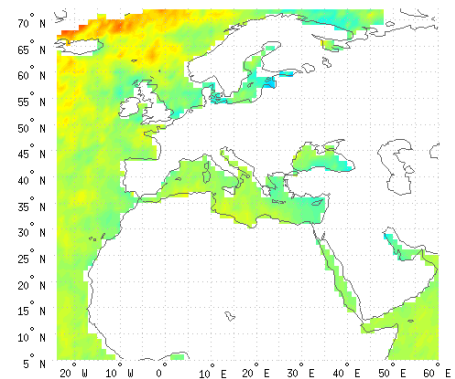
1047

(a) (b)



1048

(c) (d)



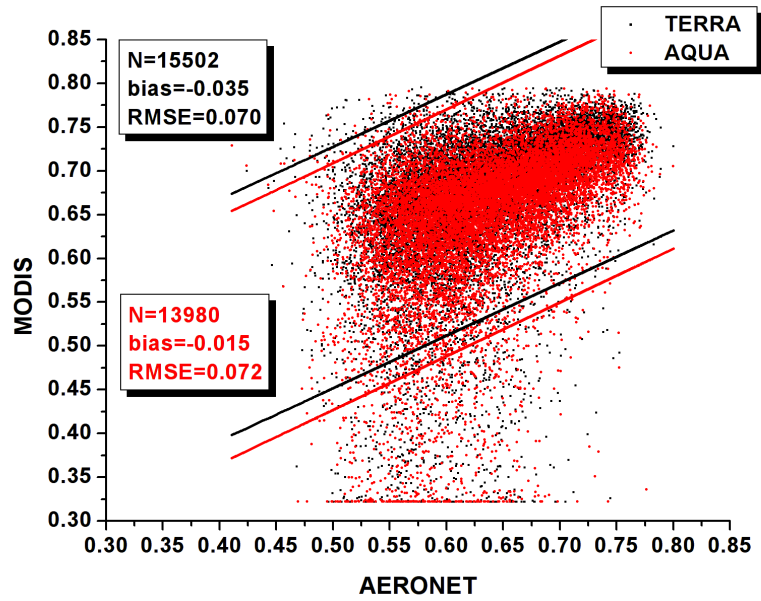
1049

(e) (f)

1050

1051 **Figure 8.** (a) Geographical distribution of MODIS-Aqua C006 Ångström exponent
 1052 (AE₅₅₀₋₈₆₅) values averaged over 2002-2010, at the wavelength pair of 550-865nm.
 1053 Winter AE data are missing from the northernmost areas and therefore the long-term
 1054 averages in (a) are left blank. In (b), (c) and (d) are given the correlation coefficients,
 1055 the absolute biases and the relative percent biases, respectively, between the C006 and
 1056 corresponding 051 AE₅₅₀₋₈₆₅ data. In (e) and (f) are given the computed

1057 deseasonalized trends of MODIS Aqua 051 and C006 AE₅₅₀₋₈₆₅) slope values for years
1058 2002-2010, respectively.
1059



1060

1061

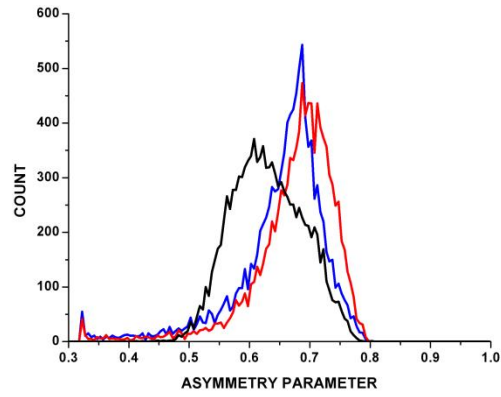
1062 **Figure 9.** Scatterplot comparison between g_{aer} values at 870 nm from MODIS Terra

1063 (black color) and Aqua (red color) and corresponding values from AERONET stations

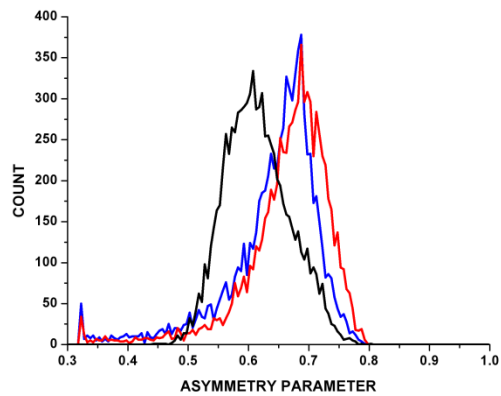
1064 at 870 nm (blue squares, Fig. 1). The 95% prediction bands as well as the mean bias

1065 (AERONET minus MODIS) and root mean squared error are given.

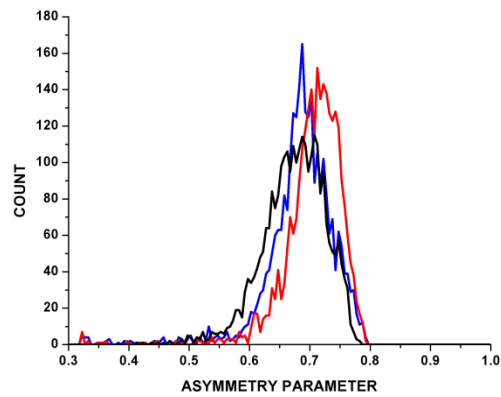
1066



(a)



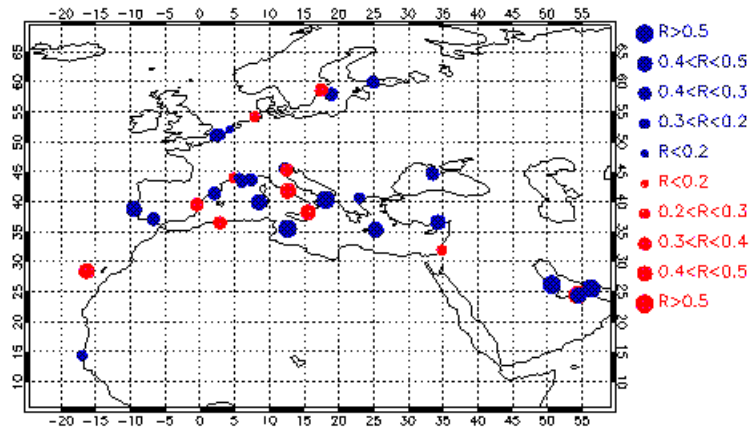
(b)



(c)

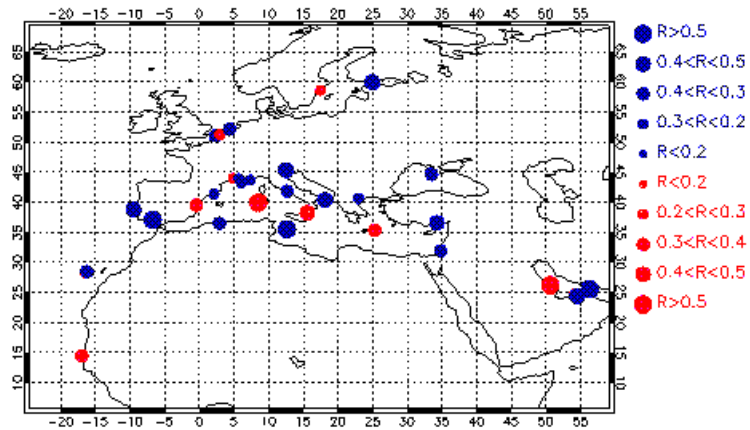
Figure 10. Frequency distribution histograms for MODIS-Terra (red colored lines) MODIS-Aqua (blue-colored lines) and AERONET (black lines) g_{aer} values at 860 and 870 nm, respectively. The histograms are given separately for: (a) the entire study region, (b) Europe and (c) Africa, Middle East and Arabian peninsula.

1078



(a)

1079



(b)

1080

1081

1082

1083

1084

1085

1086

1087

Figure 11. Map distribution of correlation coefficients between: (i) MODIS-Terra and AERONET g_{aer} values at 860 and 870 nm, respectively (left column) and (ii) MODIS-Aqua and AERONET g_{aer} values at 860 and 870 nm (right column). The size of circles corresponds to the magnitude of correlation coefficients, while blue and red colors are used for stations for which MODIS and AERONET indicate same and opposite tendency of g_{aer} , respectively.